Domain studies by x-ray and optical techniques

Midgley, D.

Domain Studies by X-ray and Optical Techniques

by

D. Midgley

Report of research conducted in the Physics department of Durham University and submitted for the degree of Doctor of Philosophy.

September, 1978

Abstract

The use of both Lang and synchrotron radiation topography for investigations of ferromagnetic domains in terbium and ferric borate, and of Jahn-Teller domains in dysprosium vanadate is described. The topographic quality assessment of flux grown rare earth aluminates and arsenates is also described, as is work on the magneto-optics of ferric borate assuming a 180^{o} Bloch wall lying perpendicular to the c-axis. A comparison of the resolution of Lang and synchrotron topography with particular reference to defects in a silicon crystal is also presented.

Acknowledgements

I wish to thank in particular Dr B K Tanner for his encouragement during the preparation of this thesis and Dr W D Corner for some valuable suggestions. Thanks are also due to Mrs B M Wanklyn and Dr S H Smith of Oxford University for supplying the crystals studied and to Mr K Moulson and Mr J Scott for manufacturing and preparing equipment for use at the Daresbury synchrotron NINA.

Publications

1. Observation of antiferromagnetic domains in $KNiF_3$ by X-ray topography : M. Safa, D. Midgley and B.K. Tanner : Phys. Stat. Sol. (a) 28, K89 (1975)

2. Observation of magnetic domain wall movements by X-ray topography using synchrotron radiation : B.K. Tanner, M. Safa, D. Midgley and J. Bordas : J. Magn. Magnetic Mater. 1, 337 (1976)

3. Cryogenic X-ray topography using synchrotron radiation : B.K. Tanner, M. Safa and D. Midgley : J. Appl. Cryst. 10, 91 (1977). Contains work from chapters 3, 4 and 6.

4. Dislocation contrast in X-ray synchrotron topographs : B.K. Tanner, D. Midgley and M. Safa : J. Appl. Cryst., 10, 281 (1977). Contains work from chapter 2.

5. Growth and perfection of rare earth aluminates and $DyFeO_3$ crystals with MoO_3 as additive. B.M. Wanklyn, D. Midgley, and B.K. Tanner. J. Cryst. Growth 29, 281 (1975) Contains work from chapter 5.

6. Flux growth and characterization by X-ray topography of rare earth arsenates, S.H. Smith, G. Garton, B.K. Tanner and D. Midgley, J. Mater. Sci. 13, 620 (1978). Contains work from chapter 5.

Declaration

Work conducted at the Daresbury Laboratories was of a joint nature and this thesis presents that part of the work particularly relevant to the author's other research.

Contents Page

1. Production and Contrast of X-ray Topographs

1.1 Introduction

In section two of this chapter we give a simple discussion of the types of contrast seen in X-ray topographs. Section three is a brief review of topographic methods under the headings of continuous and monochromatic radiation methods. This section does not include a discussion of Lang topography which, because of it's central importance in this thesis, is given a fuller treatment in section four. Section five deals with the basics of dynamical diffraction theory and the dispersion surface representation. The final section has a discussion of the contrast of section topographs as a preliminary to a consideration of the features of Lang topographs.

1.2 Orientation and Extinction Contrast

X-ray topographs are images, usually recorded on photographic emulsion, of either the surface of the crystal (in the reflection mode) or a projection of a certain volume of the crystal (in the transmission mode). Two major factors determine the intensity of the diffracted rays producing the image. The first factor is whether or not a local region of the crystal is oriented in such a way that it Bragg reflects part of the incident X-ray beam.

Obviously the range of wavelengths in the beam and the state of collimation are important parameters in this so called "orientation contrast". The second factor involved is the perfection of the crystal lattice as it varies from point to point. This will influence the scattering power and specimen absorption and produces the type of contrast known as "extinction contrast".

Consideration of the sensitivity of the various topographic techniques to these types of contrast will be aided by Figure 1. Two regions A and B are embedded in a matrix of perfect crystal C (Figure 1a). A is imperfect compared with C but has negligible misorientation, whereas B is as perfect as C but is slightly misoriented. If the topographic technique uses continuous radiation and the photographic plate is close to the specimen the area B will not be visible because there will be wavelengths within the continuous spectrum to satisfy the Bragg condition for this region (Figure 1b). A will stand out, being darker than the matrix C, because of a higher integrated reflecting power. This extinction contrast arises from two sources; firstly a greater range of wavelengths may be diffracted and secondly rays may be diffracted which are misoriented by more than the width of the perfect crystal rocking curve and are not diffracted by C. If the specimen to emulsion distance is increased then the difference in the directions of the diffracted rays from the regions B and C will be detected and

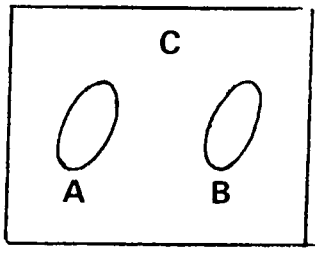

a

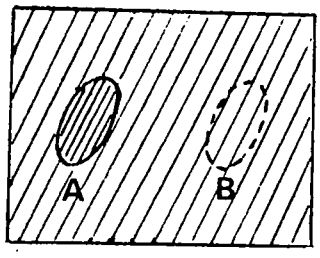

b

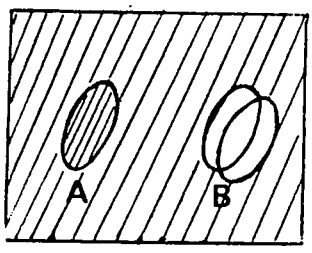

c

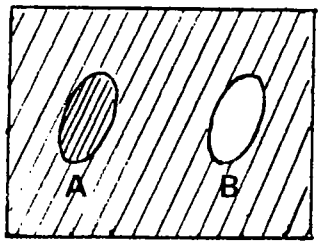

d

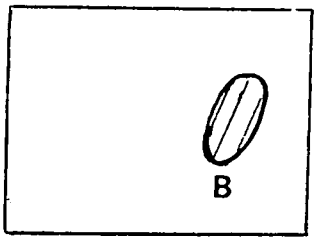

e

FIG 1

the image will appear as shown in Figure 1c. Thus the arrangement is also sensitive to orientation contrast.

If characteristic radiation is used and is collimated to such an extent that B and C may not satisfy Bragg's law simultaneously then topographs having the appearance of either 1d or 1e may be produced. In 1d the matrix C is set to diffract. A once again stands out by virtue of extinction contrast but the region B does not diffract. In 1e the region B is set to diffract. Neither A nor C will now satisfy the Bragg condition. Increasing the specimen to emulsion distance only results in poor resolution and does not alter the general appearance of either 1d or 1e.

1.3 Review of Topographic Techniques

1.3.1 Continuous Radiation Methods

In 1931 Barrett (1) pointed out that a single crystal transmission Laue diffraction spot may contain information about the internal strains in the crystal. The beam divergence and continuous spectrum together limit the resolution of these strained regions but the idea was developed by Schulz (2) in the back reflection case and by Guinier and Tennevin (3) in the transmission case.

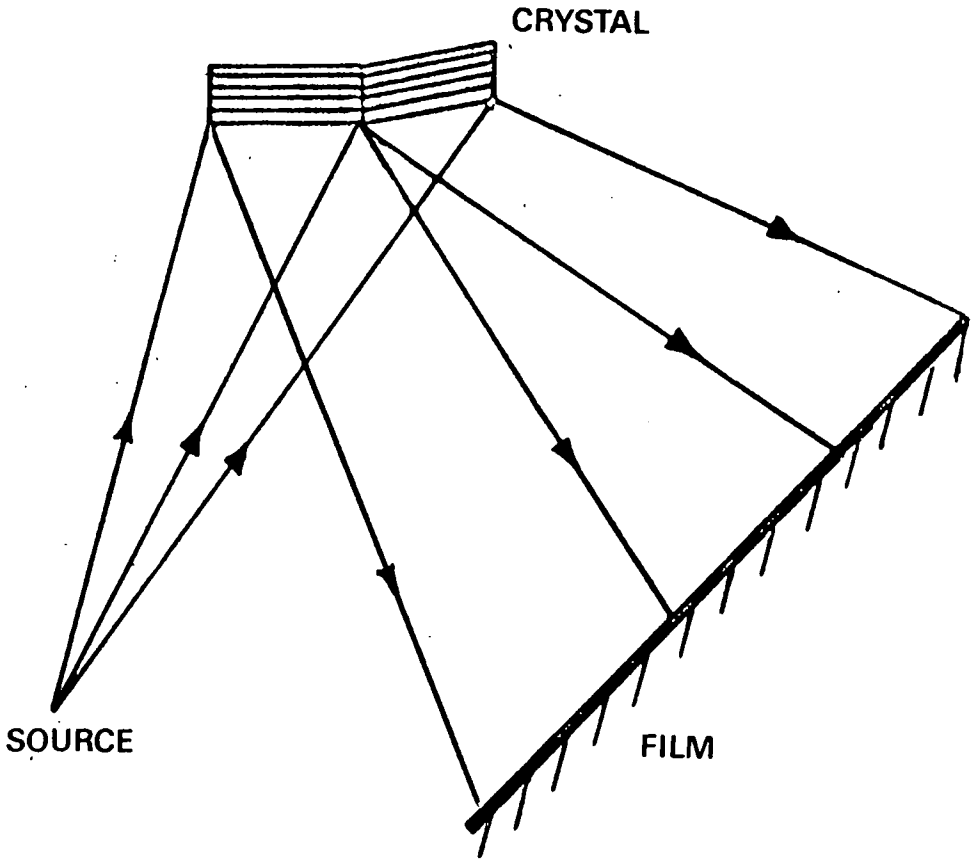

FIG 2

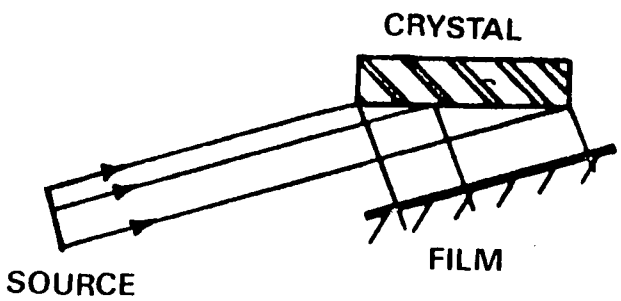

FIG 3

A typical Schulz arrangement is shown in Figure 2. Although there is little difference in the diffracted intensity from the misoriented regions, gaps and overlapping in the image allow misorientations of about 20 sec of arc to be detected. A great advantage of continuous radiation methods lies in their simplicity, a point which will be brought out more clearly in the next chapter where we discuss the use of synchrotron radiation in the Guinier - Tennevin mode.

1.3.2 Monochromatic Radiation Methods

Berg (4) and Barrett (5) developed a method using characteristic radiation and a line source. The geometry of this method is illustrated in Figure 3. The crystal is set to Bragg reflect from planes which enable the recording film or plate to be placed very close to the surface of the crystal, thus improving geometrical resolution and increasing the area of coverage. (The geometrical resolution of an arrangement is obtained simply by assuming that all rays within a beam of divergence $\Delta\theta$ may be diffracted thus yielding a range of diffracted ray angles of $\Delta\theta$. The linear resolution is thus reduced with increasing specimen to emulsion distance.) As the beam divergence of a few minutes of arc is much greater than the width of the perfect crystal rocking curve, imperfections which satisfy the Bragg condition for angles of incidence outside the range required for a perfect crystal reflection will produce dark images

against a lighter background. Misorientations of about 10-20 seconds of arc may be detected.

The double crystal technique developed independently by Bond and Andrus (6) and Bonse and Kappler (7) utilizes two successive Bragg reflections. In the most common arrangement illustrated in Figure 4 the Bragg planes are parallel and of equal spacing. For high sensitivity the specimen and reference crystal are of the same material and great care must be taken in aligning the crystals. This arrangement is non-dispersive in that all wavelengths may be diffracted with the same setting of the crystals. However any local misorientation will cause a loss in intensity. Strains of the order of 1 part in 10^7 have been detected in silicon (Hart (8)). With such high sensitivity even a carefully chosen reference crystal will not appear perfect but since it is some distance from the photographic plate these images appear less sharp than those produced by the specimen and can usually be distinguished.

1.4 Section and Lang Topography

Figure 5 serves to illustrate the experimental arrangement for both section and Lang (or projection) topography. A highly collimated line source of characteristic radiation (usually the $K\alpha_1$ line) cuts through the crystal which is set to Bragg reflect this beam from the chosen lattice

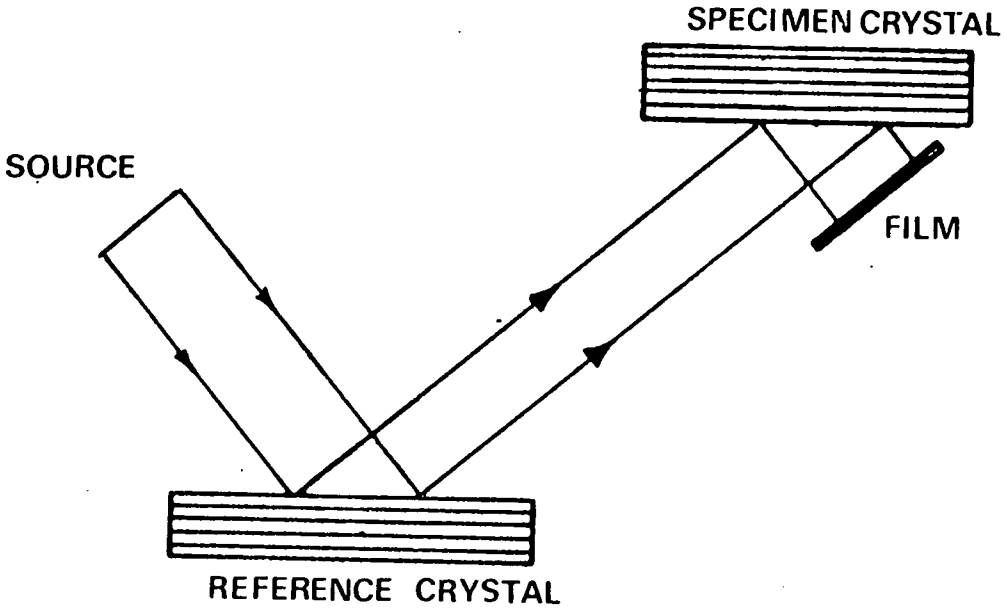
SPECIMEN CRYSTAL
SOURCE
FILM
REFERENCE CRYSTAL

FIG 4

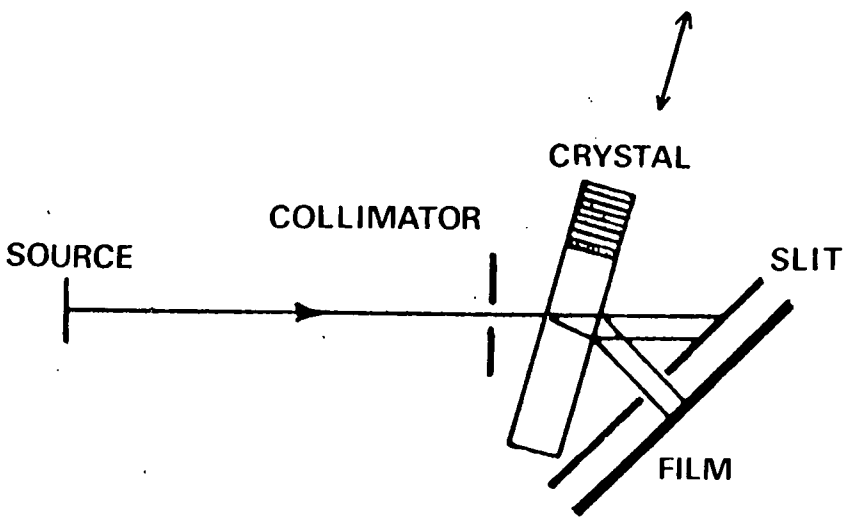
CRYSTAL
COLLIMATOR
SOURCE
SLIT
FILM

FIG 5

planes. The diffracted beam is usually detected by a photomultiplier set at twice the Bragg angle to the incident beam. A slit system is employed to shield the recording emulsion, which is usually a high resolution plate, from the intense transmitted beam. The plate is placed as close to the crystal as possible so as not to impair the geometrical resolution. For section topography the collimating slit is usually about 10μm. The reason for this choice will become apparent when we consider the formation of images in section topographs in section 1.6. In Lang topography the natural width of the characteristic line imposes a maximum resolution of about 1 μm in the plane of incidence which, for mechanical reasons, is fixed in the horizontal plane. The width of the collimating slit is chosen such that when the crystal is rotated about a vertical axis the $K\alpha_1$, and $K\alpha_2$ peaks are just resolved, thus preventing simultaneous reflection. In the vertical plane, parallel to the Bragg planes no diffraction occurs and the linear resolution is thus given by $\delta = HF/L$ where F is the specimen to plate distance, L the source to specimen distance and H the height of the source. F is usually 1-2 cm and substitution of typical values yields a resolution of a few microns.

In section topography the crystal and photographic plate are stationary whereas in Lang topography the crystal and

photographic plate are traversed repeatedly across the beam in a direction perpendicular to the diffracting planes thus covering a large area of the crystal in one exposure. Figure 44 is a photograph of a Lang camera constructed in the physics department of Durham University and shown here with a cryostat used for low temperature Lang topography (Chapter 6). The design is similar to that of a camera manufactured by Marconi-Elliot based on Lang's original design. The traversing mechanism is designed to reduce the vibration which can seriously impair resolution. The primary drive which is not mounted on the camera but on a separate board is a stepping motor controlled by a digital counter. This counter allows the change in traverse direction to be effected electronically rather than by mechanical switches on the camera itself. The stepping motor is connected directly to one of a pair of torque transmitters. This drives the second torque transmitter mounted on the camera itself. The rotation is converted to a linear motion by driving a micrometer via a set of gears which reduce the speed. The micrometer moves a table designed to hold a two arc goniometer which is supported on a set of free turning P.T.F.E. balls. The whole mechanism on the camera can be rotated about a vertical axis which is close to the axis of the goniometer. Thus once a crystal has been mounted on the goniometer with the required diffracting planes vertical, setting up an experiment is merely a matter of traversing the crystal

until it is in the X ray beam and then rotating about the vertical axis until the required Bragg reflection is detected by the photomultiplier.

For practical information on such things as the processing of photographic plates the reader is referred to an article by Lang (9) and a book by Tanner (10).

1.5 Dynamical Diffraction Theory

1.5.1 Introduction

In order to understand the contrast in topographs of thick, nearly perfect crystals, one must have some understanding of dynamical diffraction theory. The foundations of this theory were laid by Darwin (11), Ewald (12) and von Laue (13), and there has been a revival of interest over recent years as improved crystal growth techniques have produced nearly perfect crystals. Useful reviews of the subject have been given by Batterman and Cole (14), and by Hart (15).

The more familiar kinematical theory, which is adequate for thin or imperfect crystals, neglects the multiple interaction of incident and diffracted beams which is treated by dynamical theory. Each volume element contributing to the diffracted intensity is considered to be independent of the rest of the crystal except for the loss of intensity in reaching

the element and in travelling from the element to the exit surface.

The approach used here to the dynamical case is similar to that of von Laue who represented the relevant properties of the crystal by a 3-D periodic dielectric constant. Here we will use the susceptibility. Solving Maxwell's equations in this medium, using solutions consistent with the Laue equation gives a set of linear homogeneous equations for the field amplitudes, the secular determinant of which must be zero for non-trivial solutions. The dispersion surface, which represents the loci in reciprocal space of permitted wave vectors, then gives a useful representation of the main results of dynamical theory.

1.5.2 The 3-D Periodic Susceptibility

The electron density at a point $\underline{r}$ in a crystal of unit cell volume V may be represented by a Fourier sum over the reciprocal lattice vectors $\underline{g}$ as

$$\rho(\underline{r}) = (1/V) \sum_{g} F_g \exp(-2\pi j \underline{g} \cdot \underline{r}) \qquad (1)$$

where the coefficients F_g are the structure factors for reflections from planes with reciprocal lattice vectors $\underline{g}$.

Now, neglecting collisions, the equation of motion of a free electron in an electric field is

$$m\ddot{\underline{x}} = -e\underline{E} \qquad 2$$

For the interaction of an electromagnetic wave and a free electron (we assume that the K and L electrons may be considered as free), $\underline{x}$ and $\underline{E}$ may be written in the form

$$\underline{x} = \underline{x}_o \exp(-j\omega t)$$
$$\underline{E} = \underline{E}_o \exp(-j\omega t) \qquad 3$$

Substituting equations 3 in equation 2 we obtain

$$\underline{x} = \frac{e}{m\omega^2}\underline{E}$$

The polarization $\underline{P}$ is given by

$$\underline{P} = -\rho(\underline{r})e\underline{x} = \frac{-\rho(\underline{r})e^2}{m\omega^2}\underline{E}$$

and the susceptibility by

$$\chi = \frac{\underline{P}}{\varepsilon_o \underline{E}} = \frac{-\rho(\underline{r})e^2}{\varepsilon_o m\omega^2} \qquad 4$$

Substituting for $\rho(r)$ in equation 4 from equation 1 gives

$$\chi = - \frac{e^2}{\varepsilon_o m\omega^2} \left(\frac{1}{V}\right) \sum_g Fg \exp(-2\pi j \underline{g}.\underline{r}) \qquad 5$$

Also we may write

$$\chi = \sum_g \chi_g \exp(-2\pi j \underline{g}.r) \qquad 6$$

Comparing equation 5 and equation 6 we have

$$\chi_g = - \frac{e^2}{\varepsilon_o m\omega^2 V} \qquad Fg = - \Gamma Fg \qquad 7$$

1.5.3 Solution of Maxwell's Equations

Assuming that at X-ray frequencies the conductivity of the medium is zero and the permeability is unity Maxwell's equations reduce to

$$\nabla \times \underline{E} = - \frac{\partial \underline{B}}{\partial t} = -\mu_o \frac{\partial \underline{H}}{\partial t}$$

$$\nabla \times \underline{H} = \frac{\partial \underline{D}}{\partial t} = \varepsilon_o \frac{\partial (k\underline{E})}{\partial t}$$

Now we assume that the solutions may be expressed as a sum of plane waves as

$$\underline{A} = \exp 2\pi j\nu t \sum_{g} \underline{A}g \exp\left(-2\pi j \underline{K}g . \underline{r}\right)$$

Following the course previously outlined we obtain the relationship between the two wavefields of physical importance, those of the incident and diffracted beams, as

$$\alpha_o \alpha_g = \tfrac{1}{4} k^2 C^2 \chi_g \chi_{\bar{g}} = \tfrac{1}{4} k^2 C^2 \Gamma^2 F_g F_{\bar{g}} \quad \text{(From equation 7)} \qquad 8$$

where k is the vacuum wave vector and C is a polarization factor of unity for the σ polarization state (normal to the plane of incidence) and $\cos 2\theta$ for the π state (in the plane of incidence).

$$\alpha_o = \frac{1}{2k}\left[\underline{K}o . \underline{K}o - k^2 (1 - \Gamma Fo)\right]$$

and

$$\alpha_g = \frac{1}{2K}\left[\underline{K}g . \underline{K}g - k^2 (1 - \Gamma Fo)\right] \qquad 9$$

1.5.4 The Dispersion Surface

The dispersion surface which is based on the Ewald construction (see Figure 6) represents the relationship between $\underline{K}o$ and $\underline{K}g$ as described in equation 8. Referring to Figure 7 we see that circles of radius k (spheres in 3-D) have been constructed about the origin of the reciprocal lattice point 0 and about the reciprocal lattice point G.

At the intersection of these circles, the Laue point L, the relation $\underline{K}g = \underline{K}o + \underline{g}$ is satisfied for $|\underline{K}o| = |\underline{K}g| = k$.

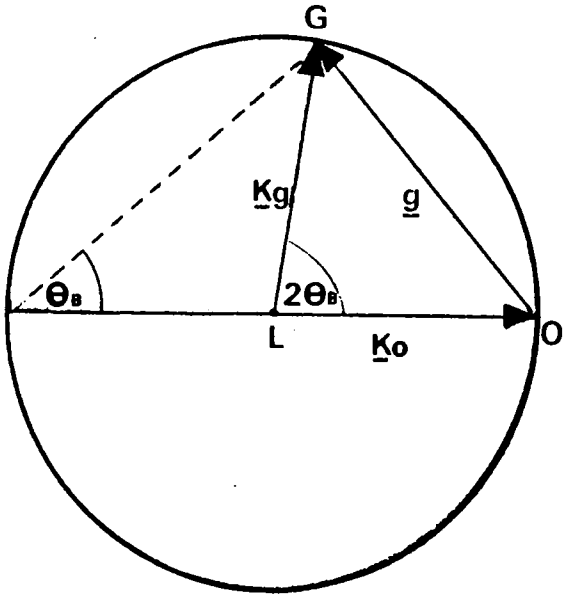

FIG 6

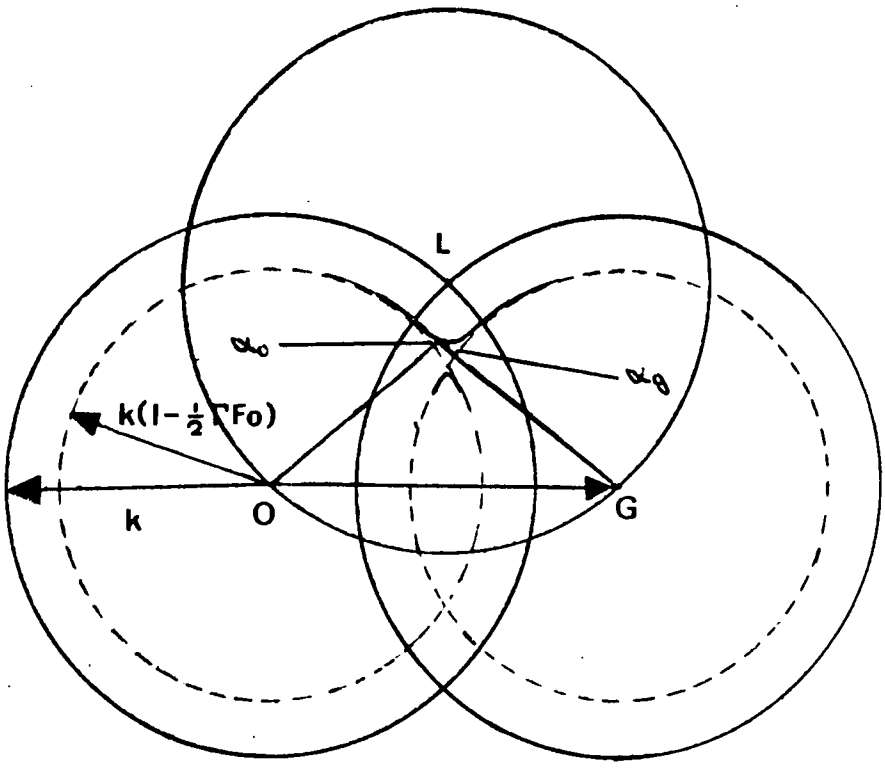

FIG 7

If we redraw the spheres for $|\underline{K}o| = |\underline{K}g| = k(1 - \frac{1}{2}\Gamma Fo)$ we take into account the average refractive index of the medium. If we rewrite the first of equations 9 as

$$\alpha_o = \frac{1}{2K}\left[(\underline{K}o.\underline{K}o)^{\frac{1}{2}} + k(1 - \Gamma Fo)^{\frac{1}{2}}\right]\left[(\underline{K}o.\underline{K}o)^{\frac{1}{2}} - k(1-\Gamma Fo)^{\frac{1}{2}}\right]$$

which, since $|\underline{K}o|$ does not differ much from k, reduces to

$$\alpha_o = (Ko.Ko)^{\frac{1}{2}} - k(1 - \Gamma Fo)^{\frac{1}{2}} \qquad 10$$

We obtain $|Ko| = k(1 - \frac{1}{2}\Gamma Fo) + \alpha_o$

Similarly $|Kg| = k(1 - \frac{1}{2}\Gamma Fo) + \alpha_g$

Thus $|Ko|$ ($|Kg|$) differs from $k(1 - \frac{1}{2}\Gamma Fo)$ by α_o (α_g) giving loci for the possible origin of $\underline{K}o$ ($\underline{K}g$) shown in figure 7 for +ve and -ve corrections (α and β branch respectively)

We are only interested in the region near the Laue point where the spheres may be approximated as planes. In Figure 8 AA′ and BB′ represent near planar sections of the spheres about O and G respectively. Figure 7 represented only one polarisation state. In Figure 8 the solid line represents the σ state and the broken line the π state. A point on one of the dispersion surface branches is called a tie point and vectors drawn from one of these tie points to O and G represent an allowed wave vector pair. α_o and α_g are in general complex so we must give some justification for discounting the imaginary parts in our discussion of the

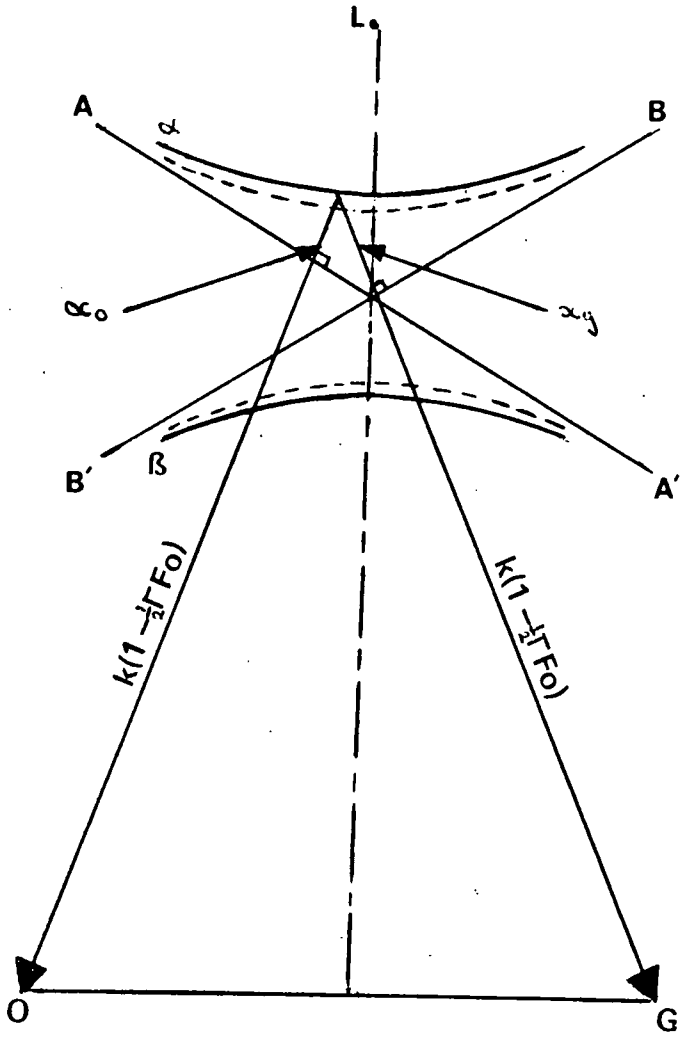
L
A
B
α
α_o
α_y
B'
ß
A'
$k(1-\frac{1}{2}\Gamma Fo)$
$k(1-\frac{1}{2}\Gamma Fo)$
O
G

FIG 8

dispersion surface. If in equation 10 we write $K_o = K_o' - jK_o''$ (where K_o'' represents the absorptive part of the wave vector) we obtain

$$\alpha_o = K_o' \left[1 - \left(\frac{K_o''}{K_o'}\right)^2 - 2j \left(\frac{K_o''}{K_o'}\right) \cos\beta \right]^{\frac{1}{2}} - k(1 - \tfrac{1}{2}\Gamma F_o)$$

where β is the angle between K_o' and K_o''. In most cases of interest $(K_o''/K_o')^2 \ll 1$ so expanding the remaining terms of the first bracket and separating real and imaginary parts we obtain,

$$\alpha_o' \triangleq K_o' - k\,(1 - \tfrac{1}{2}\Gamma F_o')$$

$$\alpha_o'' \triangleq -K_o'' \cos\beta + \tfrac{1}{2}k\Gamma F_o'' \qquad 11$$

So α_o' is practically independent of K_o'' and the dispersion surface is a valid representation of the possible wavefields in a crystal under low absorption conditions.

It may be shown by substituting back into Maxwell's equations that the ratio of the field amplitudes is given by

$$\frac{E_g}{E_o} = -\frac{2\alpha_o}{kC\Gamma F_g} = \frac{-kC\Gamma F_g}{2\alpha_g} \qquad 12$$

1.5.5 Boundary Conditions at Crystal Surface

We consider the incidence of linearly polarized plane waves on the crystal surface. The general case of polarization may be treated by the superposition of orthogonal polarization states. Spherical wave effects will be considered later. The boundary is considered plane and sharp.

As the amplitude of reflected waves at the surface is quite negligible (except at grazing incidence) the field vectors must be continuous across the surface. In addition, for the phase fronts to match across the boundary, the wave vectors inside and outside the crystal can only differ by a vector normal to the surface.

i.e. $\underline{K}o^{i} - \underline{K}o_j = k g_j \hat{n} \quad (j = \alpha\pi, \alpha\sigma, \beta\pi, \beta\sigma)$

Where $\underline{K}o^{i}$ is the incident wave vector and g_j is an "accommodation factor" which differs for each internal wave vector $\underline{K}o_j$.

We now specifically consider the Laue case of diffraction i.e. in transmission. The tie points A and B (figure 9) are found by drawing the normal to the surface SS' through the tail of Ko^{i}. Thus the "inside incident wave vectors", $Ko_{\alpha\sigma}$ and $Ko_{\beta\sigma}$ are generated.

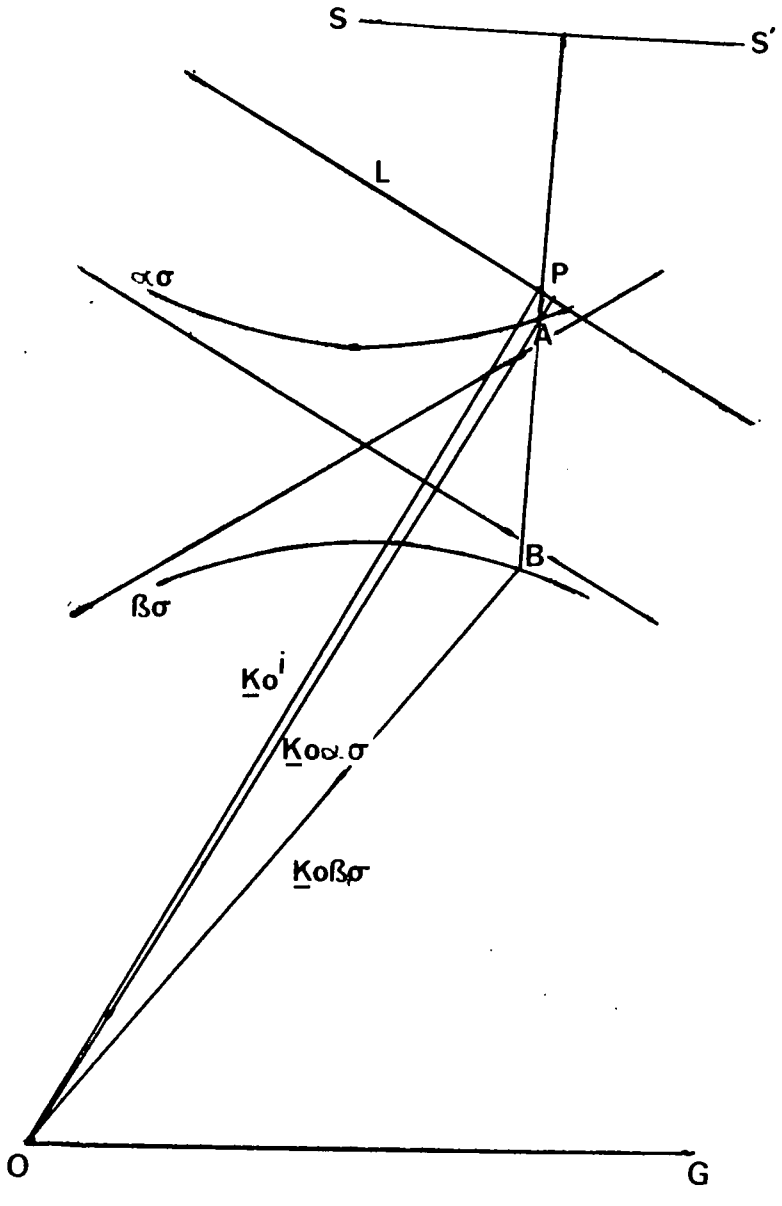
S
S'
L
P
A
B
$\alpha\sigma$
$\beta\sigma$
$\underline{K}o^i$
$\underline{K}o\omega.\sigma$
$\underline{K}o\beta\sigma$
O
G

FIG 9

Utilizing the Bragg condition $\underline{Kg} = \underline{Ko} + \underline{g}$ and dividing the wave vectors into real and imaginary parts we may write

$$\begin{aligned} \underline{Ko}^{i} - \underline{Ko}_{j}' &= kg_{j}'\hat{n} \\ \underline{Ko}_{j}'' &= kg_{j}''\hat{n} \\ \underline{Ko}^{i} - \underline{Kg}_{j}' &= kg_{j}'\hat{n} - \underline{g} \\ \underline{Kg}_{j}'' &= kg_{1}''\hat{n} \end{aligned} \qquad (13)$$

We have considered the outside incident wave vector $\underline{Ko}^{i}$ to be real. We thus see clearly that the imaginary part of $\underline{Ko}_{j}'$, $\underline{Ko}_{j}''$ is along the surface normal i.e. the absorption front is parallel to the crystal surface. Similarly for $\underline{Kg}_{j}$.

1.5.6 Field Amplitudes

The field amplitudes at any point in a crystal depend on

1. The ratio of the field amplitudes associated with the tie point.

2. The energy of the "inside incident wave" as decided by the boundary conditions.

3. The absorption of the medium.

At the exact Bragg angle the outside incident wave vector passes through the Laue point L. Referring to figure 10 we now examine what happens if this condition is not exactly met. We treat all vectors to O (or G) as parallel.

$$K_o' = k - kg_j\hat{n}.\hat{s}_o$$
$$K_g' = PG - kg_j\hat{n}.\hat{s}_g \qquad 14$$

where $\hat{s}_o$ and $\hat{s}_g$ are unit vectors in the incident and diffracted beam directions.

Now $PG = k + LP\sin 2\theta = k - k\Delta\theta\sin 2\theta$ where $\Delta\theta = LP/k$ 15

From equations 11, 14 and 15 we obtain

$$\alpha_o' = \tfrac{1}{2}k\Gamma F_o' - kg_j' \hat{n}.\hat{s}_o$$
$$\alpha_g' = \tfrac{1}{2}k\Gamma F_o' - kg_j' \hat{n}.\hat{s}_g - k\Delta\theta\sin 2\theta$$
$$\alpha_o'' = \tfrac{1}{2}k\Gamma F_o'' - kg_j'' \hat{n}.\hat{s}_o$$
$$\alpha_g'' = \tfrac{1}{2}k\Gamma F_o'' - kg_j'' \hat{n}.\hat{s}_g$$

In combined form

$$\alpha_o = \tfrac{1}{2}k\Gamma F_o - kg_j\hat{n}.\hat{s}_o$$
$$\alpha_g = \tfrac{1}{2}k\Gamma F_o - kg_j\hat{n}.\hat{s}_g - k\Delta\theta\sin 2\theta$$

We may eliminate g_j from these equations and, utilizing

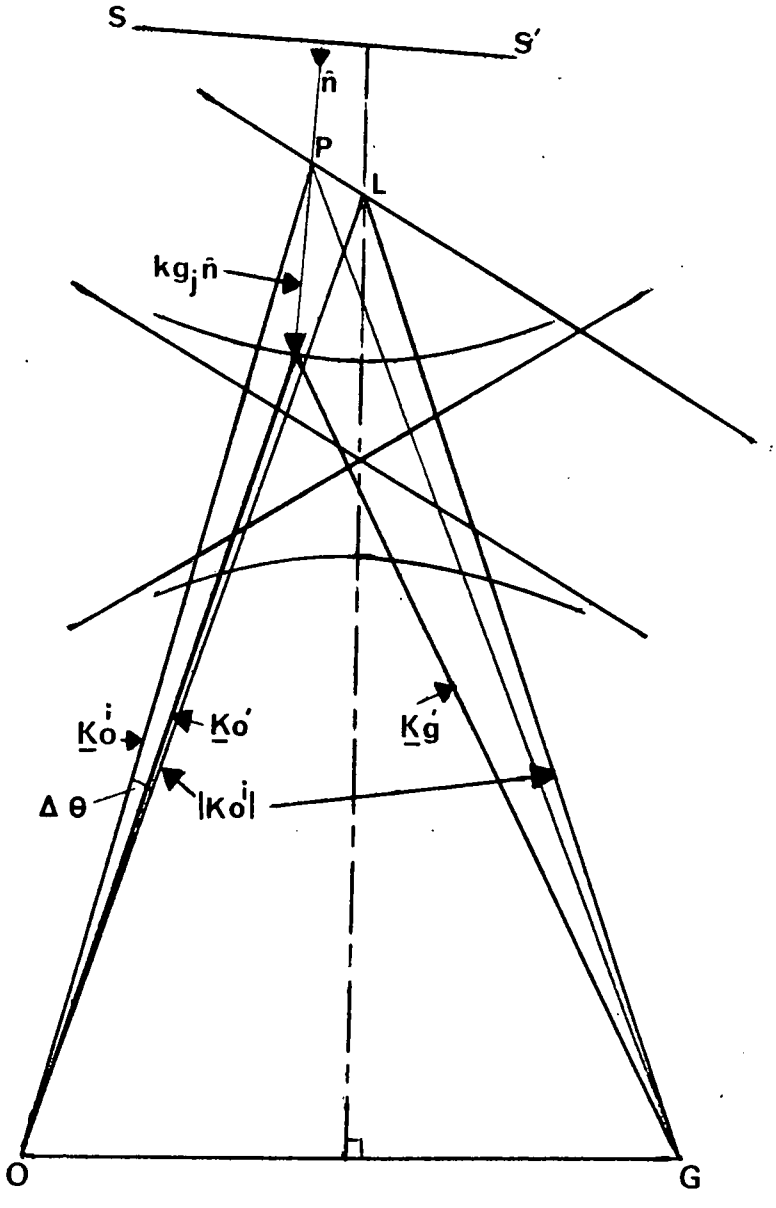

FIG IO

the equation of the dispersion surface, we obtain

$$\alpha_o^2 + \alpha_o\left(\frac{\hat{n}.\hat{s}_o}{\hat{n}.\hat{s}_g}\right)\left[\tfrac{1}{2}k\Gamma F_o\left(1 - \frac{\hat{n}.\hat{s}_g}{\hat{n}.\hat{s}_o}\right) - k\Delta\theta\sin 2\theta\right] - \tfrac{1}{4}\left(\frac{\hat{n}.\hat{s}_o}{\hat{n}.\hat{s}_g}\right) k^2C^2\Gamma^2F_gF_{\bar{g}} = 0$$

Considering a symmetric Laue reflection where $\hat{n}.\hat{s}_o/\hat{n}.\hat{s}_g = 1$ this reduces to

$$\alpha_o = \tfrac{1}{2}k\Delta\theta\sin 2\theta \pm \tfrac{1}{2}(k^2\Delta\theta^2\sin^2 2\theta + k^2C^2\Gamma^2F_gF_{\bar{g}})^{\frac{1}{2}} \qquad 16$$

Well off the Bragg angle when $\Delta\theta^2\sin^2 2\theta >> C^2\Gamma^2F_gF_{\bar{g}}$ we have

$$\alpha_o \rightarrow \tfrac{1}{2}\left[k\Delta\theta\sin 2\theta \pm k\,|\Delta\theta|\,\sin 2\theta\right]$$

i.e. $\alpha_o' = 0,\ \pm k\,|\Delta\theta|\,\sin 2\theta$

$\alpha_o'' = 0$

From equation 12 we have $E_g/E_o = -2\alpha_o/kC\Gamma F_{\bar{g}}$. Referring to figure 11 we see that for tie points A_1 and B_4 $\alpha_o \rightarrow 0$ so $E_g/E_o \rightarrow 0$. Thus there is no diffracted wave and only a single wave of amplitude Eo is propogated. For B_1 and A_4 $\alpha_o \rightarrow \infty$ and so an infinitely large Eg would occur for any Eo, suggesting that $E_o \rightarrow 0$ i.e. no incident wave can exist to excite these tie points. Near the diameter of the dispersion surface tie points on both branches are active and at the centre $|E_g| = |E_o|$ (To prove this put $\Delta\theta = 0$ remembering that $F_g \pm F_{\bar{g}}$ for any structure.)

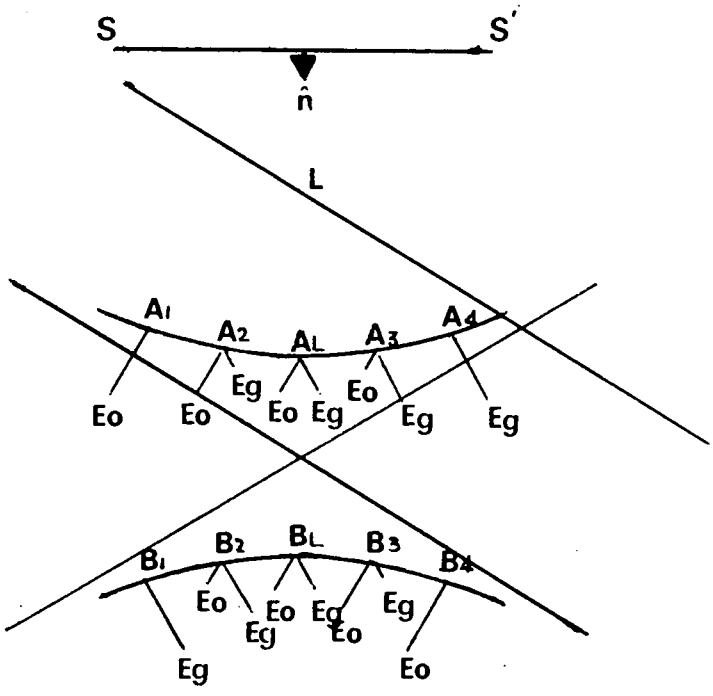
S
S'
n̂
L
A1
A2
AL
A3
A4
Eo
Eo
Eg
Eo
Eg
Eo
Eg
Eg
B1
B2
BL
B3
B4
Eo
Eg
Eo
Eg
Eg
Eo
Eg
Eo

FIG 11

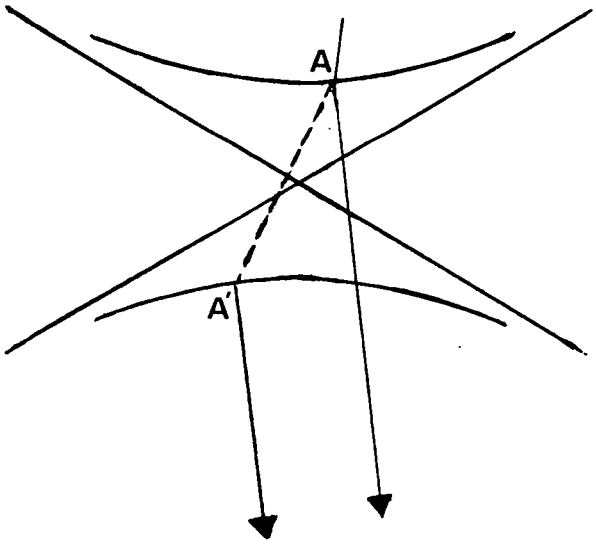
A
A'

FIG 12

1.5.7 The Energy Flow and Pendellösung Fringes

Since from a topographic point of view we are more interested in diffracted intensity than with wave vectors we now turn our attention to the Poynting vector for the total wavefield. The instantaneous Poynting vector is given by $\underline{S} = \underline{E} \times \underline{H}$ and represents the energy crossing unit area normal to $\underline{S}$ in unit time. The complexity of the wave field makes the instantaneous Poynting vector of little value so we average first over time and over the unit cell yielding a sum of these components related to the α branch, the β branch, and a coupling term between them.

$$\text{i.e.} \quad \underline{S} = \underline{S}_\alpha + \underline{S}_\beta + \underline{S}_{\alpha\beta}$$

where

$$\underline{S}_\alpha = \tfrac{1}{2}\exp(-4\pi \underline{K}''_{o\alpha}.\underline{R}) \left[|\underline{E}_{o\alpha}|^2 \hat{\underline{s}}_o + |\underline{E}_{g\alpha}|^2 \hat{\underline{s}}_g \right]$$

$$\underline{S}_\beta = \tfrac{1}{2}\exp(-4\pi \underline{K}''_{o\beta}.\underline{R}) \left[|\underline{E}_{o\beta}|^2 \hat{\underline{s}}_o + |\underline{E}_{g\beta}|^2 \hat{\underline{s}}_g \right]$$

$$\underline{S}_{\alpha\beta} = \exp\left[-2\pi(\underline{K}''_{o\alpha} + \underline{K}''_{o\beta}) .\underline{R}\right] \times$$

$$\left(|\underline{E}_{o\alpha}||\underline{E}_{o\beta}| \hat{\underline{s}}_o + |\underline{E}_{g\alpha}||\underline{E}_{g\beta}| \hat{\underline{s}}_g\right) \cos\left[2\pi (\underline{K}'_{o\alpha} - \underline{K}'_{o\beta}) .\underline{R}\right]$$

The coupling term contains the beginnings of an explanation of the so-called Pendellösung fringes which may be observed in wedge shaped crystals. Assuming for simplicity that the absorption is negligible (i.e. $\underline{K}''_{o\alpha} = \underline{K}''_{o\beta} = 0$) then $\underline{S}_\alpha$ and $\underline{S}_\beta$ are independent of depth. The vector $(\underline{K}'_{o\alpha} - \underline{K}'_{o\beta})$ is normal to the entrance surface (from boundary conditions)

so $\underline{S}_{\alpha\beta}$ is constant parallel to the entrance surface but varies sinusoidally with depth having a period $1/(K'_{o\alpha} - K'_{o\beta})$. In fact energy is exchanged back and forth between s_o and s_g as a function of depth extinguishing totally in the s_g direction and nearly in the s_o direction. The period is thus often known as the extinction distance. It may be shown that $\underline{S}_{\alpha\beta}$ is parallel to the entrance surface and so does not contribute to the energy flow through the crystal.

The net direction of energy flow is found by averaging the Poynting vector over an extinction distance i.e. for zero absorption

$$\underline{S} = \underline{S}_\alpha + \underline{S}_\beta = (|\underline{E}o_\alpha|^2 \hat{s}_o + |\underline{E}g_\alpha|^2 \hat{s}_g) + (|\underline{E}o_\beta|^2 \hat{s}_o + |Eg_\beta|^2 \hat{s}_g)$$

Kato (16) has shown that the direction of energy flow associated with a particular tie point is normal to the dispersion surface at that point. Thus for the diameter points the energy flow is along the atomic planes.

1.5.8 Limitations of Plane Wave Theory

For the plane wave theory to be truly valid the divergence of the incident wave field must be rather less than the width of the rocking curve. In fact, in most experiments this is not the case and the whole of the dispersion surface

is simultaneously excited by coherent radiation. Thus wave fields are produced which fill the 2θ range between s_0 and s_g, thus lying in a triangle which is sometimes known as the Bormann fan.

In the previous section we noted that the coupling term $S_{\alpha\beta}$ predicted the possibility of Pendellösung fringes. In fact, in cases where the plane wave approximation is valid, such fringes are not often observed because the wave fields from the two branches of the dispersion surface do not superpose in the crystal. If, however, the whole of the dispersion surface is excited, interference may occur between tie points such as A and A' (figure 12) where the surface normals are in the same direction.

1.5.9 Absorption

The imaginary part of α_0 is given by equation 11 as

$$\alpha_0'' \simeq -K_0'' \cos\beta + \tfrac{1}{2}k\Gamma F_0''$$

As we have seen, well off the Bragg angle $\alpha_0'' \to 0$ so that $K_0''\cos\beta = \tfrac{1}{2}k\Gamma F_0''$. Thus the exponential absorption factor is given by

$$\exp(-2\pi \underline{K}_0'' \cdot \underline{R}) = \exp\left[-2\pi(\tfrac{1}{2}k\Gamma F_0'')t\right]$$

Squaring the term on the right to represent an intensity loss and equating to $\exp(-\mu_o t)$ where μ_o is the linear absorption coefficient we have

$$\mu_o = 2\pi k \Gamma F_o''$$

For the diameter points ($\Delta\theta = 0$) we have from equation 16

$$\alpha_o'' = \pm \tfrac{1}{2} k |C| \Gamma I [F_g F_{\bar{g}}]^{\frac{1}{2}}$$

where I indicates the imaginary part. Moving away from the exact Bragg angle an increasingly large real part is added to the complex constant before taking the square root. The effective absorption coefficient is proportional to the difference between the linear absorption line $\frac{1}{2} k \Gamma F_o''$ and α_o'' for the $\Delta\theta$ value of interest, (figure 13). Thus we see that the α branch can have a very small absorption coefficient. The physical explanation of this so-called anomalous transmission is illustrated in figure 14, for diameter points on the dispersion surface where Eo = Eg. Standing wave patterns are set up in which the atomic planes coincide with nodes of the α branch and antinodes of the β branch. Thus for the α branch σ polarization the electric field at an atomic site is zero so that no absorption can occur. The π polarization state suffers absorption because the $\cos 2\theta$ term prevents the electric field from going to zero at the atomic sites.

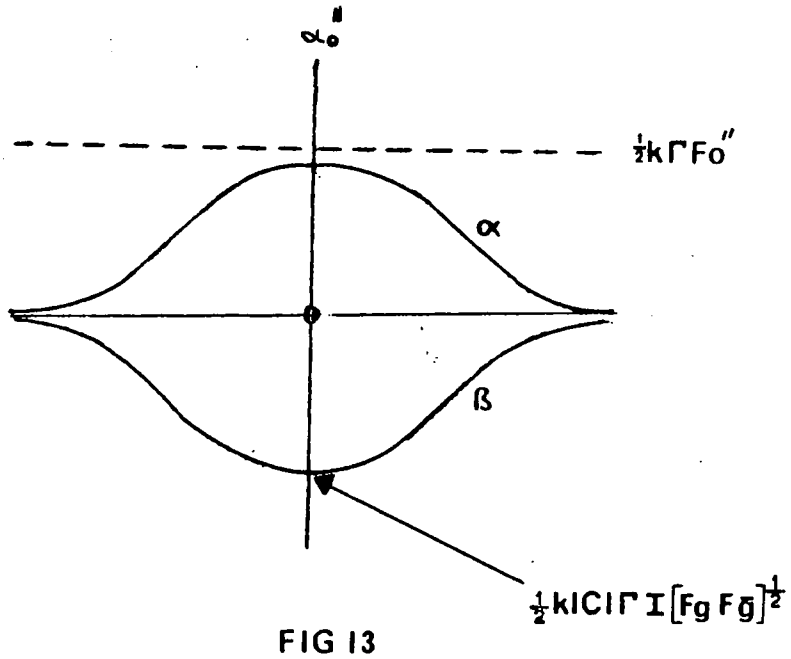
α_o''
$\frac{1}{2}k\Gamma Fo''$
α
β
$\frac{1}{2}kIC|\Gamma I[Fg\,F\bar{g}]^{\frac{1}{2}}$

FIG 13

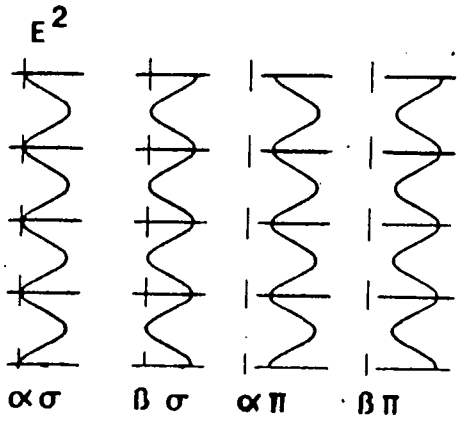
E^2
$\alpha\sigma$
$\beta\sigma$
$\alpha\pi$
$\beta\pi$

FIG 14

1.6 The Contrast of Dislocation Images in Section and Lang Topography

Having, from the previous section, gained some understanding of the wavefields within the Borrmann fan we are now in a position to discuss the contrast of dislocation images in section topographs and to relate this to the case of Lang topographs. First of all, however, we will point out that some valuable information is lost in Lang topographs. Referring to figure (15) we see that a stationary arrangement with a collimating slit narrow compared with BC will record the distribution of energy within the Borrmann fan, information which is lost if the crystal and plate are traversed or if the width of the collimating slit becomes comparable with BC. The latter is the reason for the narrow slit used when taking section topographs. The detailed nature of the energy distribution within the fan need not concern us here, suffice it to say the Pendellösung fringes may be observed in crystals with parallel exit and entrance surfaces, an observation predicted by the spherical wave dynamical diffraction theory of Kato (17) and that averaging over the period of the Pendellösung Fringes enhanced intensity is found at the edge of the diffracted beam.

Three types of dislocation image may occur simultaneously in section topographs. The "direct" image i_1 (figure (16)) arises from the reflection of part of the direct beam by the strained region around a dislocation core. Since the part

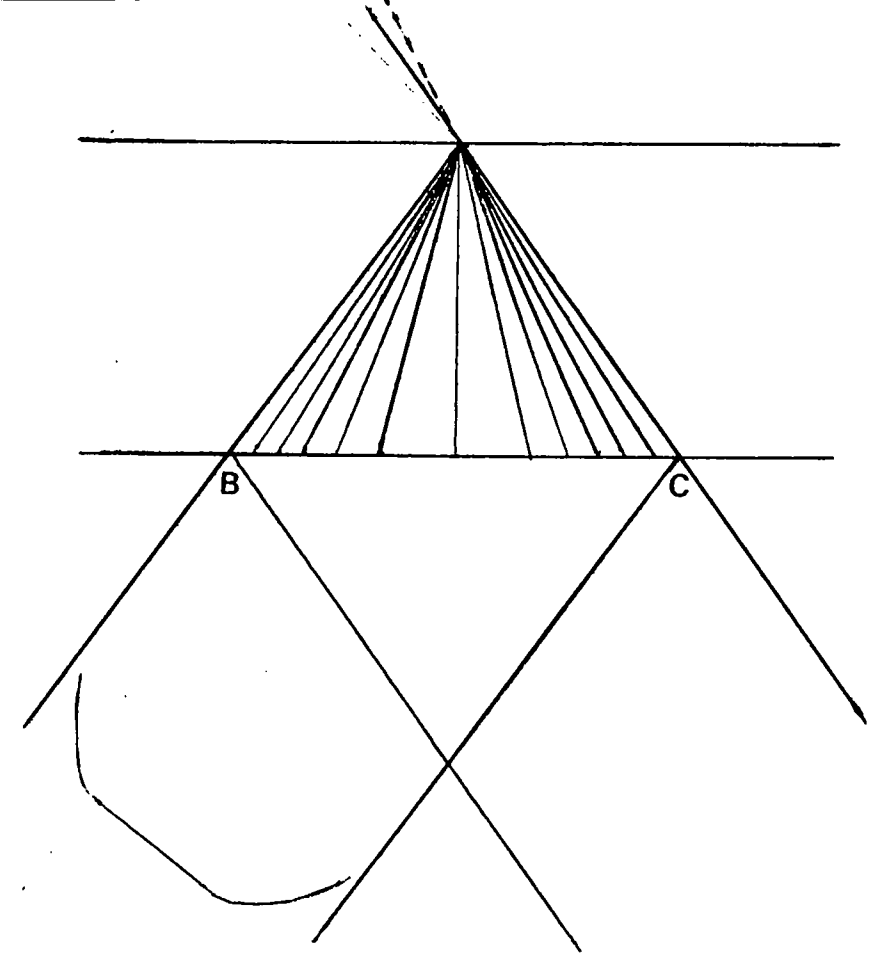

FIG 15

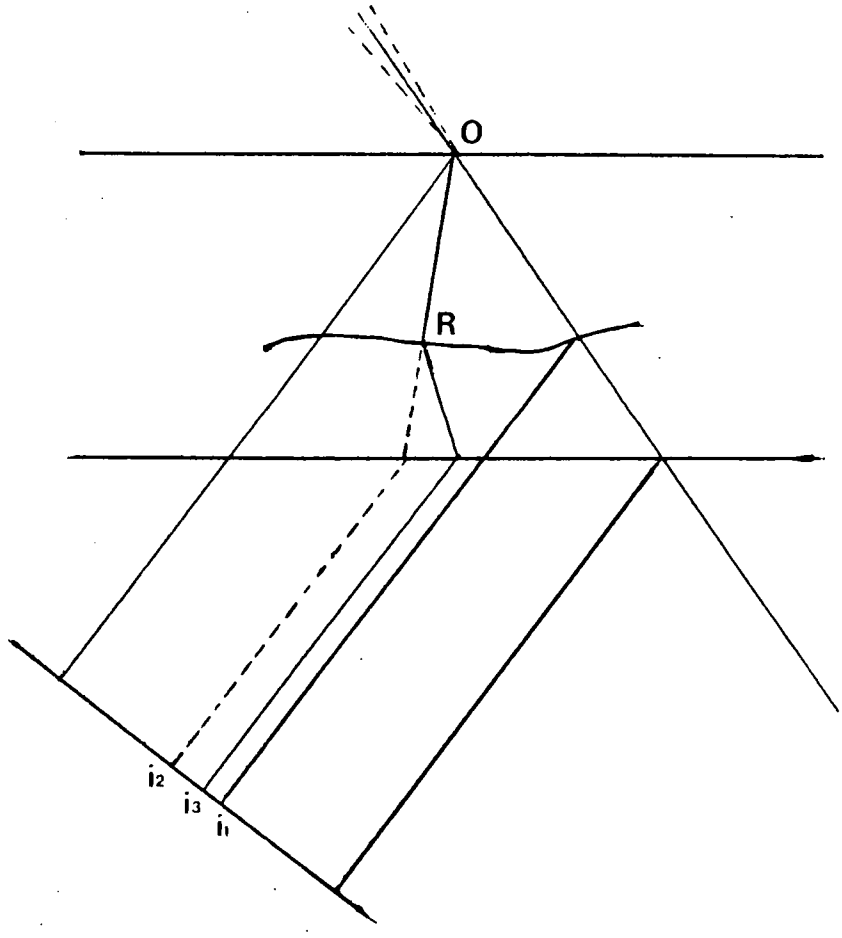

FIG 16

reflected must lie well away from the centre of the perfect crystal reflecting range for the dislocation image to be distinguished, the linear absorption is dominant and, in thick crystals, direct images may not appear at all. As wavefields propogating in a particular direction (say OR) within the fan enter the strained region they may decouple into transmitted and diffracted components. On re-entering the perfect crystal new wavefields are excited and energy is lost from the direction OR, thus producing a "shadow" of reduced intensity within the fan. This shadow gives rise to the "dynamic" image i_2 which appears lighter than the background on the topograph. The new wavefield interferes with the original wavefields giving rise to fringes which constitute the third type of image, the "intermediary" image i_3.

Lang topographs may be regarded as a superposition of section topographs. Once again direct images are found under conditions of reasonably low absorption. Dynamical and intermediary images tend to be blurred out. In fact intermediary images tend only to show their existence by producing an asymmetry in the dynamical images and examples of intermediary images in Lang topographs are rare.

We have here only given a brief account of the formation of dislocation images in X-ray topographs. More detailed information will be introduced as required as will

information on other features such as precipitates, domains etc.

2 Synchrotron Radiation Topography

2.1 Properties of Synchrotron Radiation

The accelerated electrons in an electron synchrotron emit electromagnetic radiation. The instantaneous power emitted by an electron of energy E travelling in a circular orbit of radius R, per unit wavelength interval, per unit of the angle ψ between the emitted radiation and the orbital plane, is given by

$$\frac{\partial^2 I(\lambda,\psi,E)}{\partial\lambda\,\partial\psi} = \frac{27}{128\varepsilon_o\pi^4}\frac{e^2c}{R^3}\left(\frac{\lambda_c}{\lambda}\right)^4\left(\frac{E}{mc^2}\right)^8\left[1+\left(\frac{E}{mc^2}\psi\right)^2\right]^2 \times \left\{K_{\frac{2}{3}}^2(\eta) + \frac{\left(\frac{E}{mc^2}\psi\right)^2}{1+\left(\frac{E}{mc^2}\psi\right)^2} K_{\frac{1}{3}}^2(\eta)\right\} \quad (1)$$

where $$\lambda_c = \frac{4\pi R}{3}\left(\frac{mc^2}{E}\right)^3$$

and $$\eta = \frac{\lambda_c}{2\lambda}\left[1+\left(\frac{E}{mc^2}\psi\right)^2\right]^{3/2}$$

The K's are modified Bessel functions of the second kind; ε_o is the permittivity of free space.

The first and second terms in the wavy brackets represent respectively the components of the emitted radiation polarized in, and normal to the orbital plane. Thus the radiation emitted in the orbital plane, for which $\psi = 0$ is horizontally plane polarized.

The spectral distribution is found by integrating equation 1 over ψ to obtain

$$\frac{\partial I(\lambda,E)}{\partial \lambda} = \frac{9\sqrt{3}}{64\pi^3\varepsilon_o R^3}\frac{e^2 c}{}\left(\frac{E}{mc^2}\right)^7\left(\frac{\lambda_c}{\lambda}\right)^3\int_{\lambda_c/\lambda}^{\infty} K_{5/3}(\eta)d\eta \qquad 2$$

The qualitative features of the synchrotron radiation spectrum are described by equation 2 although in calculating actual spectra such corrections as allowing for linear field free sections and for the fact that the instantaneous electron energy has a sine squared dependence must be made. The time averaged flux for NINA is shown in figure 17.

The radiation passes through a tangential beam pipe with a beryllium window into the experimental area (figure 18). A system of pneumatically operated shutters in the pipe allows control from outside the experimental area. The pipe is about 47m long in NINA. Betatron oscillations lead to an effective source size of 0.5mm square and at 47m this leads to a highly collimated beam 5 mm high extending horizontally around the synchrotron. Its practical width is limited by

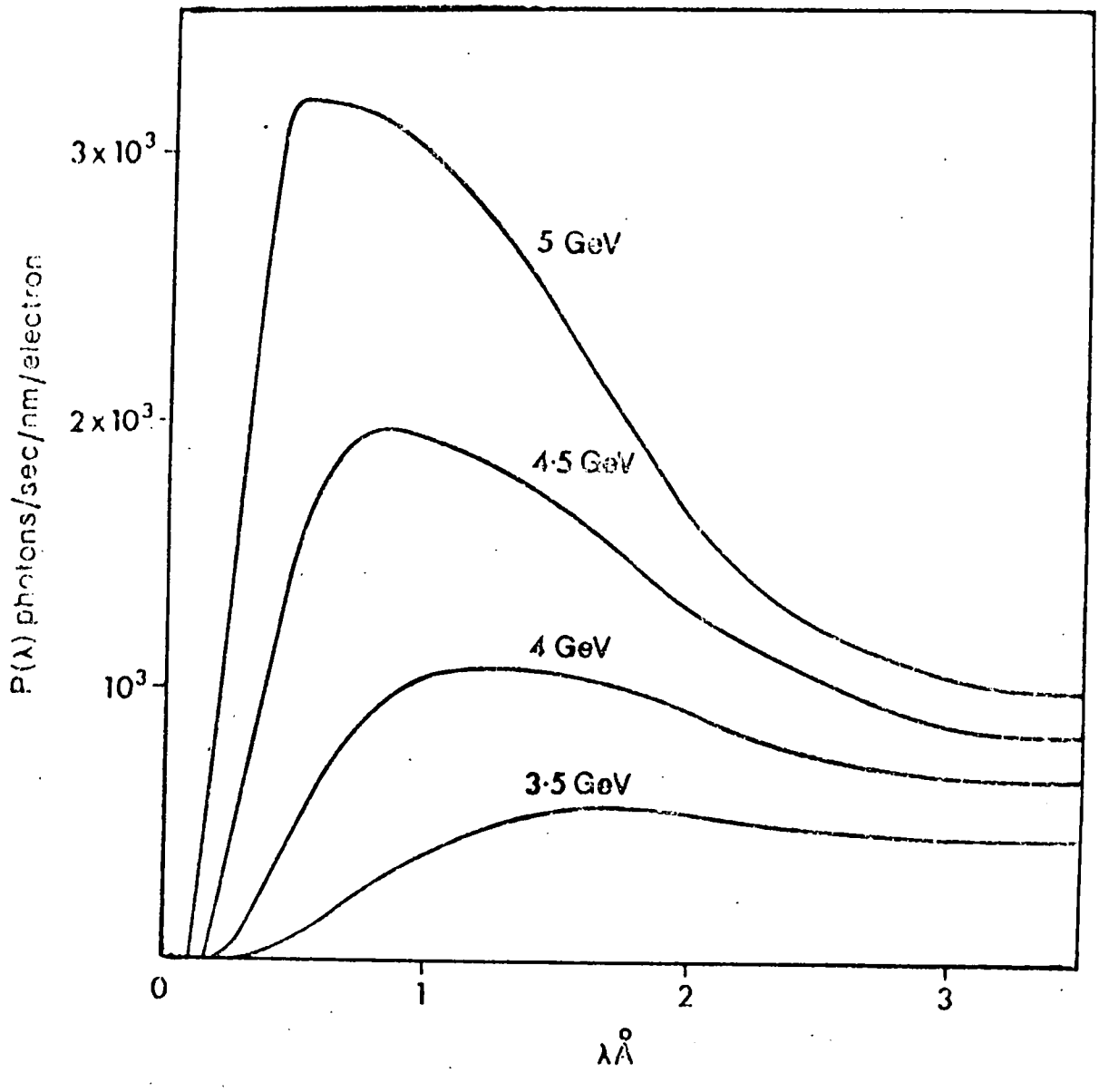
3 x 10³
2 x 10³
10³
P(λ) photons/sec/nm/electron
5 GeV
4·5 GeV
4 GeV
3·5 GeV
0
1
2
3
λÅ

FIG 17

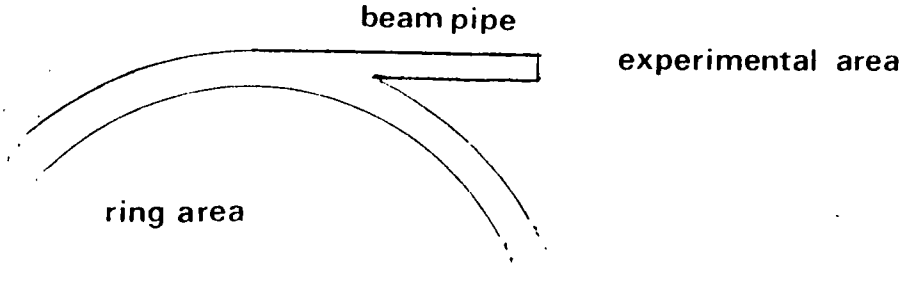
beam pipe
experimental area
ring area

FIG 18

the diameter of the beam pipe.

2.2 Uses of Synchrotron Radiation in X-Ray Topography

The advantages of synchrotron radiation as a source for X-ray topography stem from three properties; the high intensity, the continuous spectrum and the high state of collimation of the beam.

As we have seen in the first chapter, the resolution of white radiation topographs, taken using conventional X-ray sources, is rather poor. In continuous radiation topography the whole source contributes to the diffracted intensity for any part of the crystal. Consider a vertical plane of incidence. At the centre of the beam the range of possible angles of incidence on the crystal at a distance L from the source of height H, $\Delta\theta$ is H/L radians. The diffracted beam has a divergence of H/L radians yielding a vertical resolution of HF/L where F is the specimen to plate distance. Similarly for a horizontal plane of incidence, the horizontal resolution being given by WF/L where W is the source width. With W = H = 0.5 mm, L = 47 m, and F = 10 cm, the geometrical spacial resolution is just about 1μm, which is comparable with Lang topography even for the large specimen to plate distance of 10 cm.

The continuous spectrum obviates the need for the careful adjustment of the specimen which is necessary in Lang topography. One may, by adjusting the crystal, select a particular wavelength to be diffracted by a certain set of planes, and this may be desirable to improve resolution, but essentially producing a simple room temperature synchrotron topograph is no more difficult than recording a Laue diffraction pattern.

The instrumental simplification resulting from the continuous spectrum, coupled with an acceptable large specimen to plate distance makes it possible to surround the specimen with a variety of equipment such as magnets, straining jigs etc., which is difficult if not impossible when using a Lang camera. The high speed, arising from not only the high intensity but also from the fact that the whole crystal is exposed at once, makes dynamical experiments such as studies of domain wall movement, annealing of polycrystalline samples (for which the continuous spectrum is extremely useful) etc., much more feasible. These sort of studies have previously been the province of workers using powerful X-ray generators and televisions equipped with X-ray sensitive phosphor screens. In such experiments instantaneous results are gained at the expense of resolution.

One obvious advantage of the continuous spectrum is that many reflections may be recorded on one plate at the same time. This considerably eases the determination of Burger's vectors and the distortion directions in domains.

2.3 Review of Synchrotron Topography Experiments

The use of synchrotron radiation in X-ray topography was first reported by Tuomi et al in 1973 (18). Since so few results have been published then it is possible and worth while to give a brief review of individual papers.

In a subsequent paper (19) Tuomi and his co-workers discussed the results given in their first paper and of further experiments in some detail. Transmission topographs of (111) silicon were used to illustrate some possibilities and problems of the technique. After a comparison of calculated and observed diffraction spot intensities they turned their attention to individual dislocation images. For several of these they made complete Burger's vector analyses. The dislocation images were very wide because of superposed high order reflections. These have long extinction distances and, since kinematical diffraction theory gives the image width of a dislocation as $(\xi/2\pi)\ |\underline{g}.\underline{b}|$ for screw and as $(0.88\xi/\pi)$ $|\underline{g}.\underline{b}|$ for edge type, high order reflections may dominate if they are of sufficient intensity. They used Kodak R single

coated film mounted normal to the incident beam.

Hart, (20) taking surface reflection topographs, endeavoured to improve the resolution by using Ilford L4 25μm. plates mounted normal to the diffracted beam. (For high resolution work the thickness of the photographic emulsion becomes of some importance. If a beam of width d hits an emulsion of thickness t at an angle θ to the normal to the plate then the image width is given by $t \times \tan\theta + d/\cos\theta$. He also took care in limiting background radiation produced by objects (such as the goniometer) which, if hit by the beam will scatter and fluoresce. He examined oxide edges in silicon. Overlapping orders still made the images broader than when examined by Lang topography. An examination of a cleaved lithium fluoride crystal showed the possibility of using the technique on materials with many sub-grains which could not be imaged simultaneously using monochromatic radiation. The effects of the variation of emulsion sensitivity and of air absorption with wavelength on different orders were considered, factors which Tuomi's group apparently overlooked.

Bordas et al (21) illustrated the simplicity of the technique for taking topographs through a phase transition. Using a furnace consisting of a copper block heated by soldering iron elements they were able to study the

ferroelectric-paraelectric phase transition in $BaTiO_3$. During each exposure of 10-30 seconds the temperature variation was within 0.25°C.

2.4 Experiments on Silicon Wedge

A specimen of $(\bar{1}1\bar{1})$ silicon polished into a wedge of angle 1.4° with a thickness varying from 5 μm. to 120 μm. was used in a comparison of the contrast of Lang and synchrotron topographs under conditions such that higher order reflections in the synchrotron topographs were of little importance. To limit the amount of scattered and fluorescent radiation falling on the plate the beam size was reduced to 5 mm. using a drilled lead block. This was followed by a steel plate backed with aluminium with a slightly larger hole, this being used to absorb the scattered and fluorescent radiation produced by the lead collimator itself. The specimen was mounted with wax on a standard two arc goniometer. Since the intensity of the synchrotron X-ray output is very high no adjustments to the specimen may be made when the shutters are raised. To ensure that the crystal is in the path of the X-ray beam the following procedure was adopted. Two sheets of a special X-ray sensitive paper are aligned approximately with the beam, one at say 1 m. from the beam pipe, the other at say 5 m. These are then exposed and, without changing their position, pin holes are made in them

at the centre of the exposed region.* A laser at say 8 m. is then aligned along the axis of the X-ray beam using these pin holes. Not only can the specimen then be correctly positioned using the laser but also in the transmission mode the direction of the beam reflected from the crystal surface will give the direction of a symmetrical diffracted beam thus helping in locating the photographic plate. This only applies, of course, if the back surface of the crystal is normal to the Bragg planes. Figure 19 shows a synchrotron topograph of the silicon wedge recorded on L4 25 m. emulsion with a specimen to photographic plate distance of 5 cm. Figure 20 is a Lang topograph of the same wedge. Using a rotating anode generator operating at 50 kV, 40 mA with a molybdenum target the exposure time was 20 minutes on L4 50 μm emulsion as compared with 80 seconds at 5 GeV, 18 mA for the synchrotron topograph.

2.5 Contrast of Lang and Synchrotron Topographs

Apart from dislocation contrast which we will shortly

* This paper was produced by Dr. G. P. Williams of Montana State University. Essentially it consists of PVC and a pH indicator. The incident X-rays ionize the PVC. Chlorine combines with hydrogen in the film to lower the pH this being the cause of a change in colour of the dye indicator from green to purple.

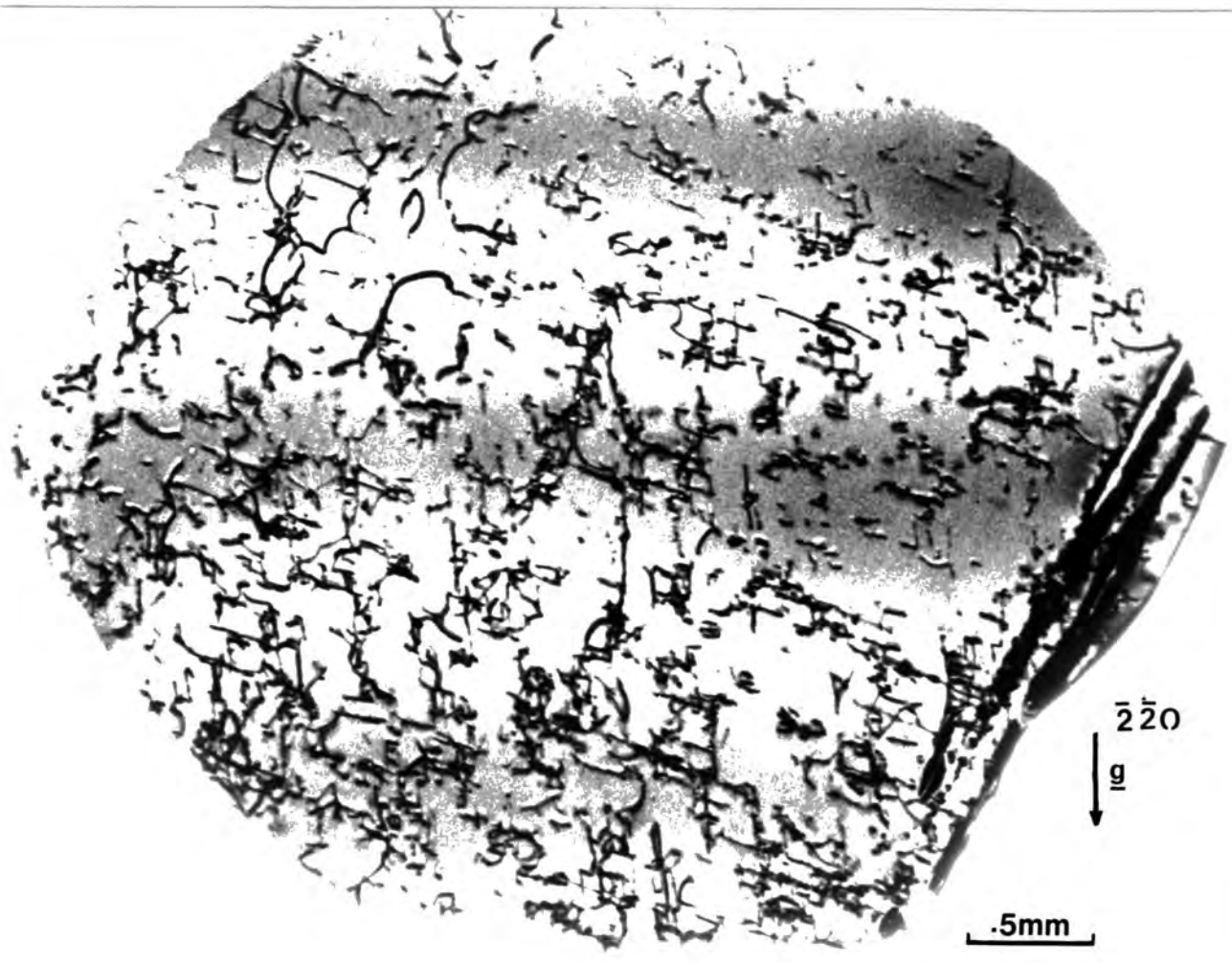

FIG 19

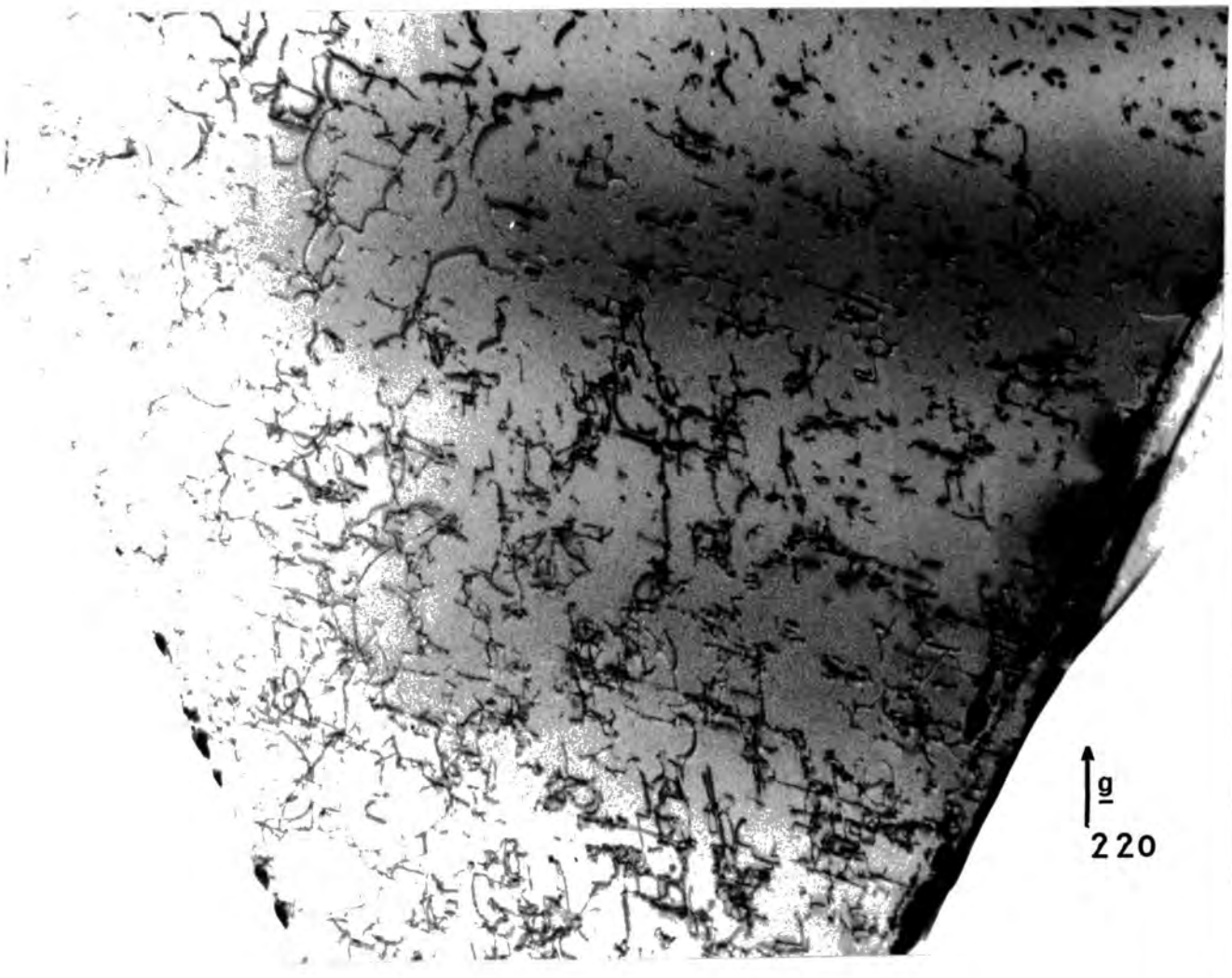

FIG 20

consider in some detail there are two striking differences between the Lang and synchrotron topographs.

1. The region N of the crystal is cracked and part of the crystal is misoriented with respect to the bulk of the crystal. The diffraction condition for this region is not satisfied in the Lang topograph but is satisfied when using synchrotron radiation. In subsequent synchrotron topographs at specimen to plate distances of 10 cm. and 20 cm. the gap was respectively twice and four times the width of the gap in the topographs shown. This illustrates the importance of orientation contrast in synchrotron topographs.

2. The fading of Pendellösung fringes results from the beating of the two modes of polarization. This occurs in the Lang topographs, but does not appear in the synchrotron topograph because of the highly polarized source. Superposition of high order reflections may produce some fading but the choice of the 220 reflection minimizes this because the 440 component contributes less than 5% to the intensity and the 660 reflection less than 0.1%.

Since one of the chief advantages of synchrotron radiation topography is that large specimen to plate distances are acceptable it is of interest to know how far this distance may be increased before resolution is seriously impaired.

We have considered geometrical resolution for a perfect crystal and this seems to suggest that at 10 cm. a resolution of about 1 - 2 μm is possible whereas at 20 cm. this is reduced to 2 - 3 μm. We will now consider the effect of orientation contrast when the crystal has misoriented regions with particular reference to the silicon wedge.

Direct and dynamical images are visible in both Lang and synchrotron topographs, highlighted by the dark Pendellösung maxima. The widths of the direct images are similar in the two topographs, the narrowest being about 8 μm., and some double images are visible in both.

In Lang topographs the small specimen to plate distance makes it possible to assume that X-rays diffracted from the misoriented region around a dislocation emerge parallel to those diffracted by the perfect crystal. This is not possible in synchrotron topographs as is vividly illustrated in figure 21 which shows sections of the synchrotron topographs taken with specimen to plate distances of 5 cm., 10 cm., and 20 cm. The dislocation images are broadened and the effect of orientation contrast in those showing double contrast is particularly striking. The effective misorientation of regions producing the two images is given by $2\alpha\theta_{\frac{1}{2}}$ where the constant α is approximately unity, and $\theta_{\frac{1}{2}}$ is the width at half height of the perfect crystal rocking curve (Authier (22)).

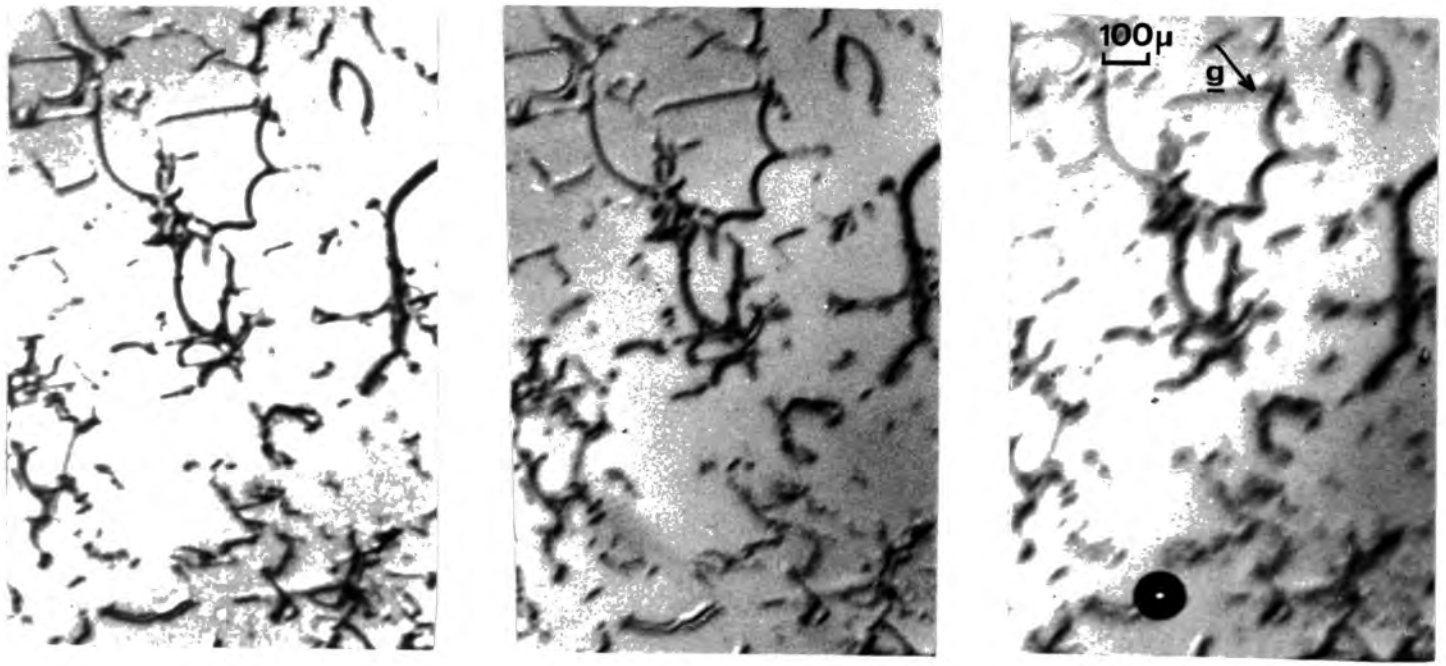

FIG 21

Thus, since the beam divergence is negligible, the angular divergence of the image maxima is $4\alpha\theta_i$. In Lang topography, where the diffraction condition for the misoriented regions is met by X-rays of the same wavelength but differing angles of incidence, the divergence of the image maxima is only $2\alpha\theta_i$. In the synchrotron case, for a $\bar{2}\bar{2}0$ reflection in silicon using radiation of about 0.96Å, the calculated divergence is 5.7×10^{-5} radians. Measurements from the three topographs of figure 21 yield a divergence of $12\ (\pm 3) \times 10^{-5}$ radians. Orientation contrast may be used to determine the sense of a Burger's vector. Using the criterion for the disappearance of an image that $|\underline{g}.\underline{b}|=0$ (where $\underline{b}$ is the Burger's vector), the Burger's vector of the dislocation A has been found to lie in the $[110]$ direction (Tanner (23)). For a double image to occur in the 220 reflection the criterion $|\underline{g}.\underline{b}| \geq 2$ must be met, giving a probable Burger's vector of $\pm \frac{1}{2}[\bar{1}\bar{1}0]$. The divergence of the lobes in the synchrotron topographs with a $(\bar{1}\bar{1}\bar{1})$ exit surface indicates that the sign is positive.

Figure 22 shows a topograph of $HoVO_4$ which indicates vividly the streaking of images produced by orientation contrast which is very common in synchrotron topographs. In this case a large distortion of the lattice has been produced by the mounting of the specimen. Excessive orientation contrast like this can be very troublesome

FIG 22

when interpreting results as will be seen in chapter 6.

2.6 Conclusion

Although, variation of the effective source size during exposure did sometimes hinder good resolution, under good conditions high resolution topographs with narrow dislocation images can be produced with synchrotron radiation. The contrast of Lang and synchrotron topographs is very similar except where large strains are present. Direct and dynamical images are seen and the sense of a dislocation Burger's vector may be determined from the divergence of double images.

3 Cryogenic X-ray Synchrotron Topography

3.1 Introduction

As indicated in the previous chapter the properties of synchrotron radiation make possible dynamic experiments on crystals which undergo phase transitions. In this chapter we describe the construction and use of three simple cryostats for use with liquid nitrogen and a cryostat manufactured by the MERIC company specifically for Lang topography which has a controllable temperature in the liquid helium range. Where examples of topographs produced using these cryostats are not shown they may be found in the paper by Tanner, Safa and Midgley. (24).

3.2 Glass Cryostat with Enclosed Cold Finger

Figure 23 shows a cryostat which was previously used to produce Lang topographs of antiferromagnetic domains in $KNiF_3$ (Safa, Midgley and Tanner(25)). For this purpose a stand was constructed to support the cryostat on a Lang camera but here it is illustrated, as it was later used for synchrotron topography, mounted on the coils of an electromagnet. At the time of construction little work on low temperature topography had been reported perhaps due to the high price of sophisticated commercially available equipment. The home built cryostat described here is

useful for experiments at about 120°K where temperature control is not essential. Attempts were made to use the cryostat at liquid helium temperatures and, although unsuccessful, it is felt that improvement to the vacuum may make this possible.

A copper rod acting as a cold finger was screwed onto a plate brazed to the copper end of a glass to metal seal. The specimens were mounted on a brass holder which could be tilted about a horizontal axis. This simple goniometer was attached to a brass rod which fitted into a hole drilled along the axis of the cold finger, the latter being equipped with a clamping screw to hold the brass rod in place. Thus a small amount of vertical adjustment was possible, this being very convenient for positioning the crystal in the beam. Larger vertical adjustment could be made by jacking up the table holding the magnet. The glass tube attached to the glass to metal seal forms the wall of the inner vessel incorporated for liquid helium use. As can be seen in Figure 23 three larger concentric tubes form the liquid nitrogen vessel and the outer of the vacuum jacket, the latter being terminated just above the specimen holder in a ground glass flange. A glass cap with a matching ground flange could be fitted over the specimen holder, thus sealing the space between the inner and outer glass walls and allowing evacuation of the cryostat. This cap was equipped with mylar windows sealed in place with epoxy resin. The

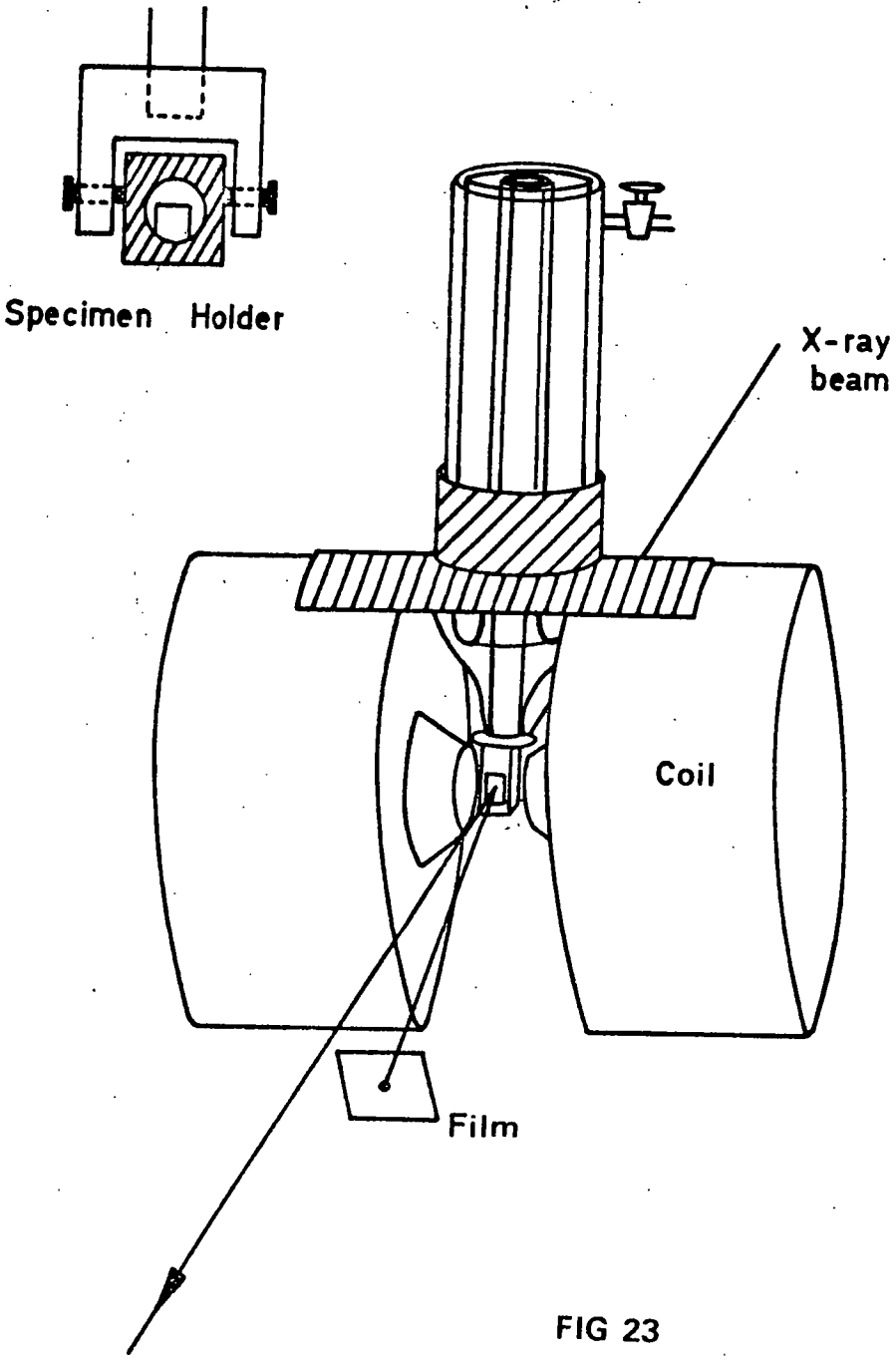

FIG 23

design of the cap was such that for Lang topography the photographic plate could be placed within 2 cm. of the specimen. The adjustments to the specimen in both Lang and synchrotron experiments were made before fitting the cap and evacuating the cryostat. With both the central and outer vessel filled with liquid nitrogen the temperature at the specimen holder was estimated to be around 120°K. This estimate was based on an attempt to measure the temperature using a copper-constantan thermocouple connected to tungsten rods passing through the wall of the cap. However emf's generated at the tungsten to copper or constantan junctions made the result unreliable.

An example of a synchrotron topograph of antiferromagnetic domains in $KNiF_3$ taken using this cryostat may be found in the paper by Safa, Tanner and Midgley (24). In Chapter four of this thesis we show as an example of the use of this cryostat a topograph showing ferromagnetic domains in a single crystal of terbium.

3.3 Meric Stainless Steel Cryostat

After the measure of success achieved with the home built glass cryostat funds became available from the Science Research Council to buy a variable temperature cryostat manufactured by MERIC for Lang topography at around liquid

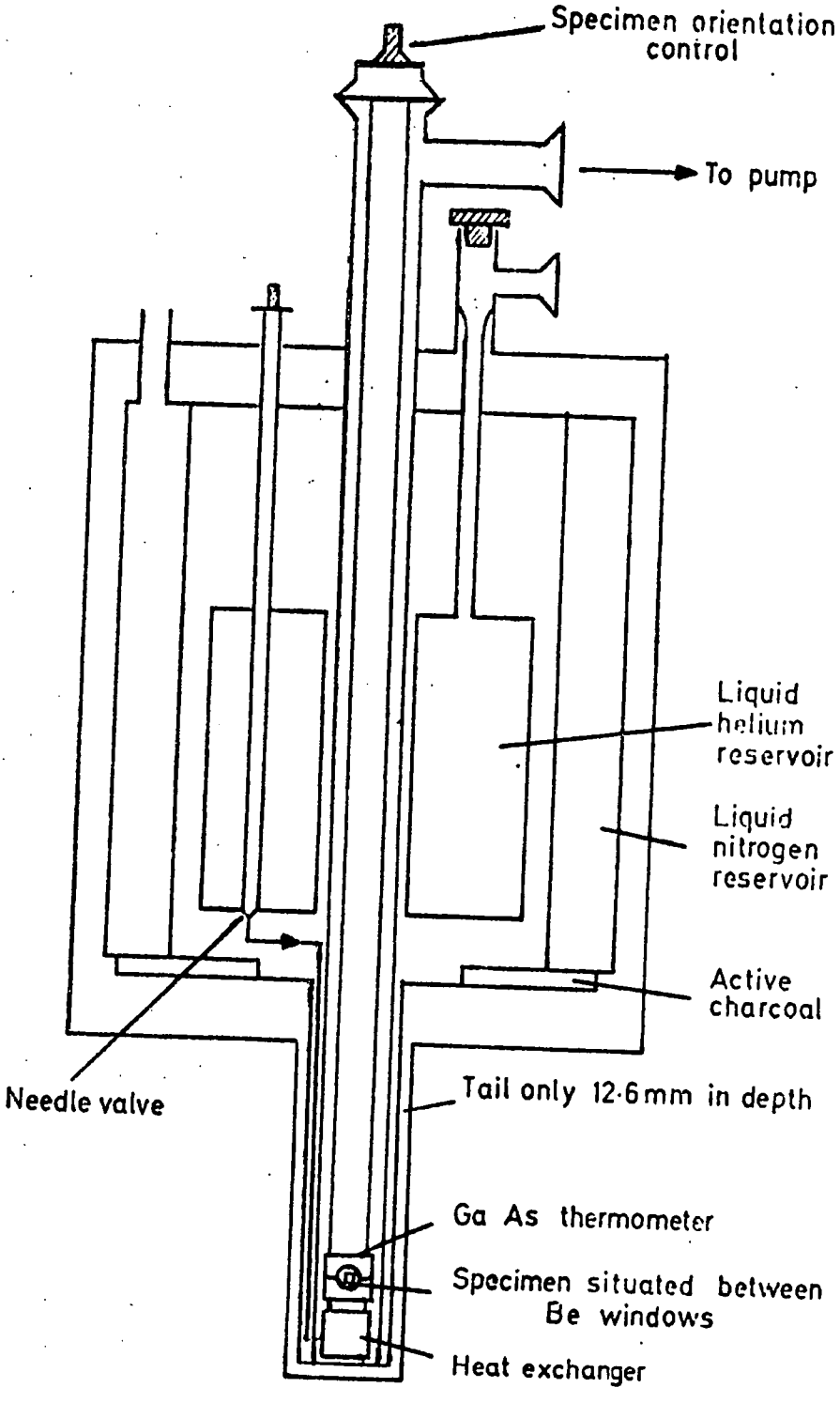
Specimen orientation control
To pump
Liquid helium reservoir
Liquid nitrogen reservoir
Active charcoal
Needle valve
Tail only 12·6mm in depth
Ga As thermometer
Specimen situated between Be windows
Heat exchanger

FIG 24

helium temperatures (Figure 24). A similar cryostat has been used for studies of magnetic domains in terbium iron garnet down to 4.2°K. (Mathiot, Petroff and Bernard, (26); Petroff and Mathiot, (27); Mathiot and Petroff, (28)). This cryostat is also shown in figure 25 mounted between the pole pieces of an electromagnet as it was used for synchrotron topography. Cooling is achieved by drawing helium vapour through a tube connecting the liquid helium reservoir and the specimen chamber, the flow being controlled by a needle valve. The helium reservoir has a capacity of 2 litres and lasts for 10 - 12 hours under steady conditions. Temperatures slightly below 4.2°K may be achieved by hard pumping and a heating element may be used to achieve temperatures in excess of 4.2°K. The temperature is stabilized at the desired level by a controller which regulates the power delivered to the heater and the speed of the pump. A GaAs diode thermometer is used to measure the temperature. It is perhaps worth while noting here that in experiments in moderate magnetic fields no unusual behaviour in the diode was indicated.

The tail of the cryostat which contains the specimen holder is only about 1.3 cm. thick, making possible, when used for Lang topography, specimen to plate distances of about 1 cm. The X-ray windows are of beryllium brazed to the steel.

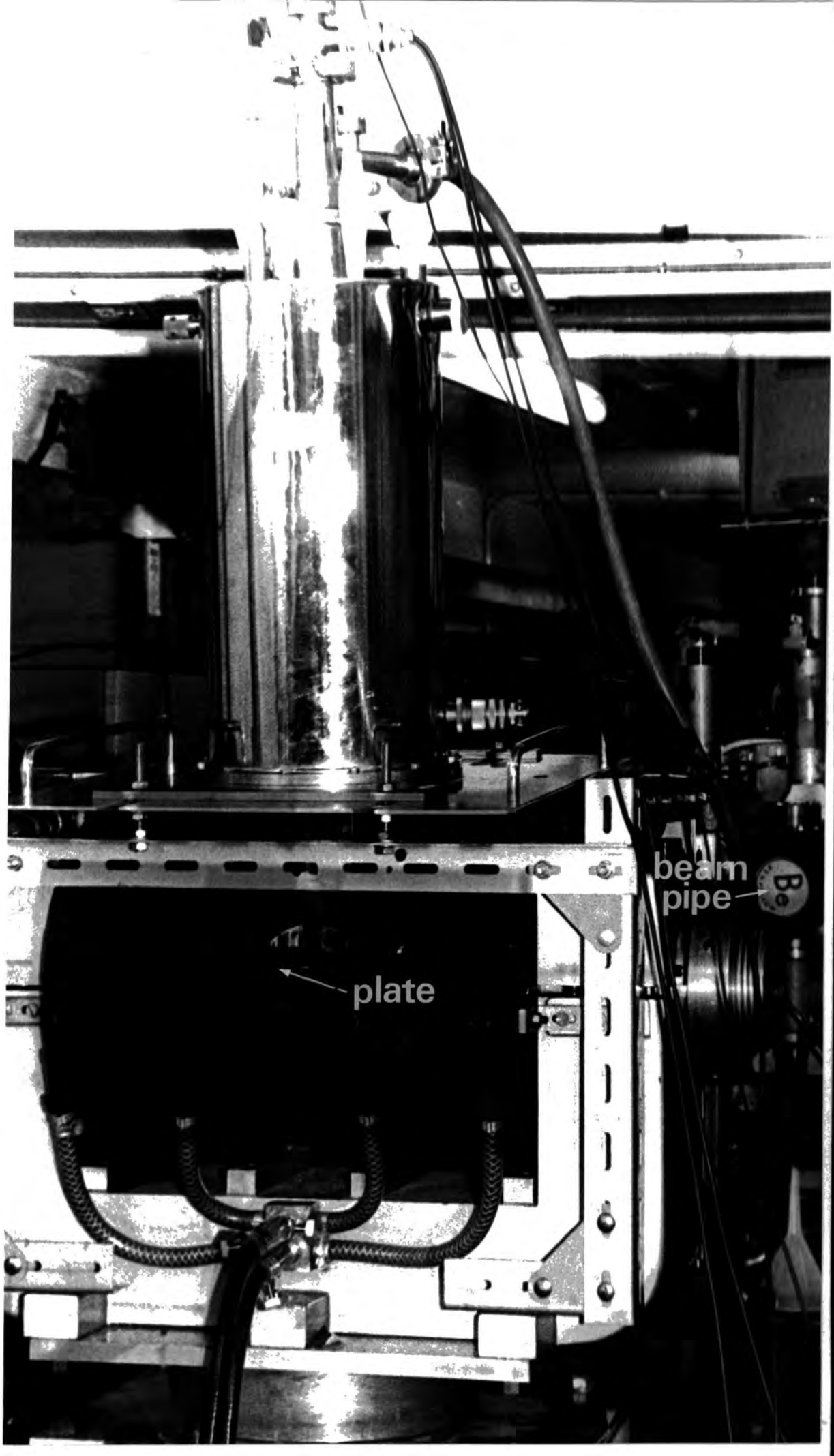

FIG 25

Examples of topographs produced using this cryostat are given in Chapter six of this thesis and in (24).

3.4 Glass Cryostat with no X-ray Window

The tail of the MERIC cryostat is rather broad, limiting the fields obtainable with the electromagnet used to about 0.7 tesla. Studies of antiferromagnetic domain wall motion in $KCoF_3$ made higher fields desirable and the simplest solution, in the absence of a more powerful electromagnet was to reduce the gap between the pole pieces. Use of the tailed glass dewar shown in figure 26 allowed the gap to be reduced to about 2 cm. As the tail was unsilvered the method of aligning the crystal using a laser described in the last chapter could be used even with the specimen immersed in liquid nitrogen. The sample was attached to a simple brass holder fixed at the end of a stainless steel rod, this being clamped at the plate covering the top of the cryostat. The liquid nitrogen bubbled continuously and violently when the specimen holder was in place, due to the conduction of heat down the stainless steel rod, but the specimen did not vibrate unacceptably. An example of a topograph of $KCoF_3$, showing an antiferromagnetic domain wall is given in (24). This paper also includes some discussion of the absorption of liquid nitrogen and glass as a function of wavelength. Above 0.7 Å a very marked absorption

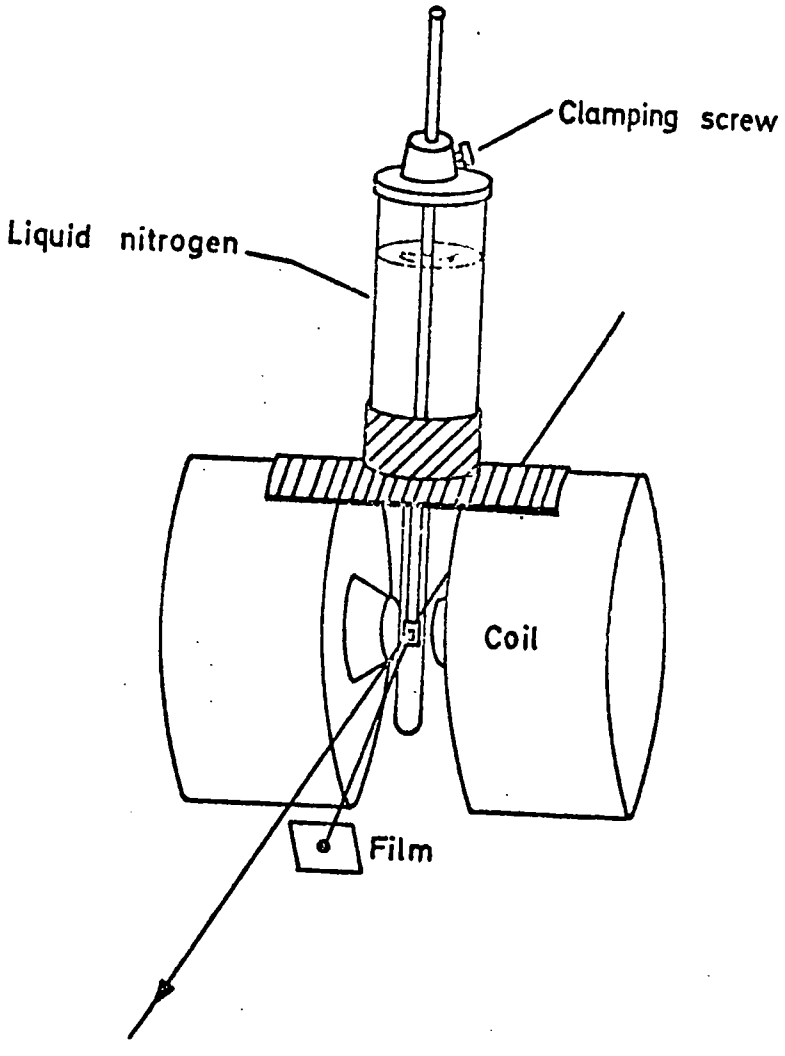

FIG 26

occurs in the glass so the Bragg angle is selected to avoid this problem. Exposure times are increased by a factor of about twenty for all Bragg angles, an increase which is acceptable with the high intensity of the synchrotron source. Typically this involves an exposure time of about 6 min.

3.5 Polystyrene Immersion Cryostat

For producing rapid results in zero fields the polystyrene cryostat described here is very useful. It is simply a trough made from polystyrene. A rod holding the specimen is supported with a clamp stand (figure 27). All adjustments to the specimen are made before bringing the trough up from underneath the specimen. Once again violent bubbling occurs but apparently causes no obvious deterioration of resolution. The nitrogen path was quite long, about 3 cm. but despite this produced a four fold decrease in exposure time over that required using the long tailed glass cryostat.

Figure 28 is a room temperature topograph of a crystal of $KCoF_3$ mounted on the supporting rod before cooling; figure 29 is of the same crystal when immersed in liquid nitrogen. The resolution of the dislocations indicates that vibration is not a serious problem. Diffuse domain images are visible

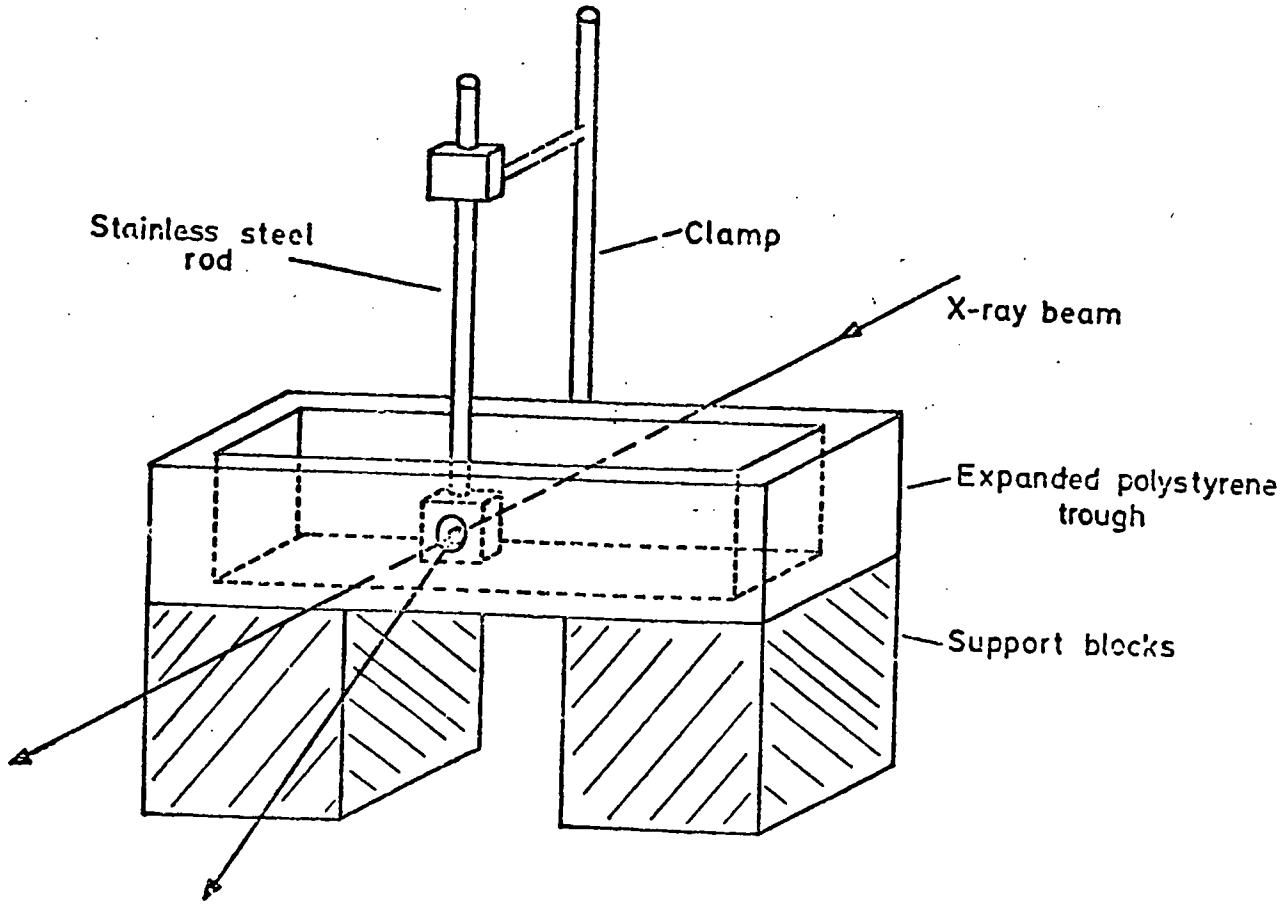
Stainless steel rod
Clamp
X-ray beam
Expanded polystyrene trough
Support blocks

FIG 27

FIG 28

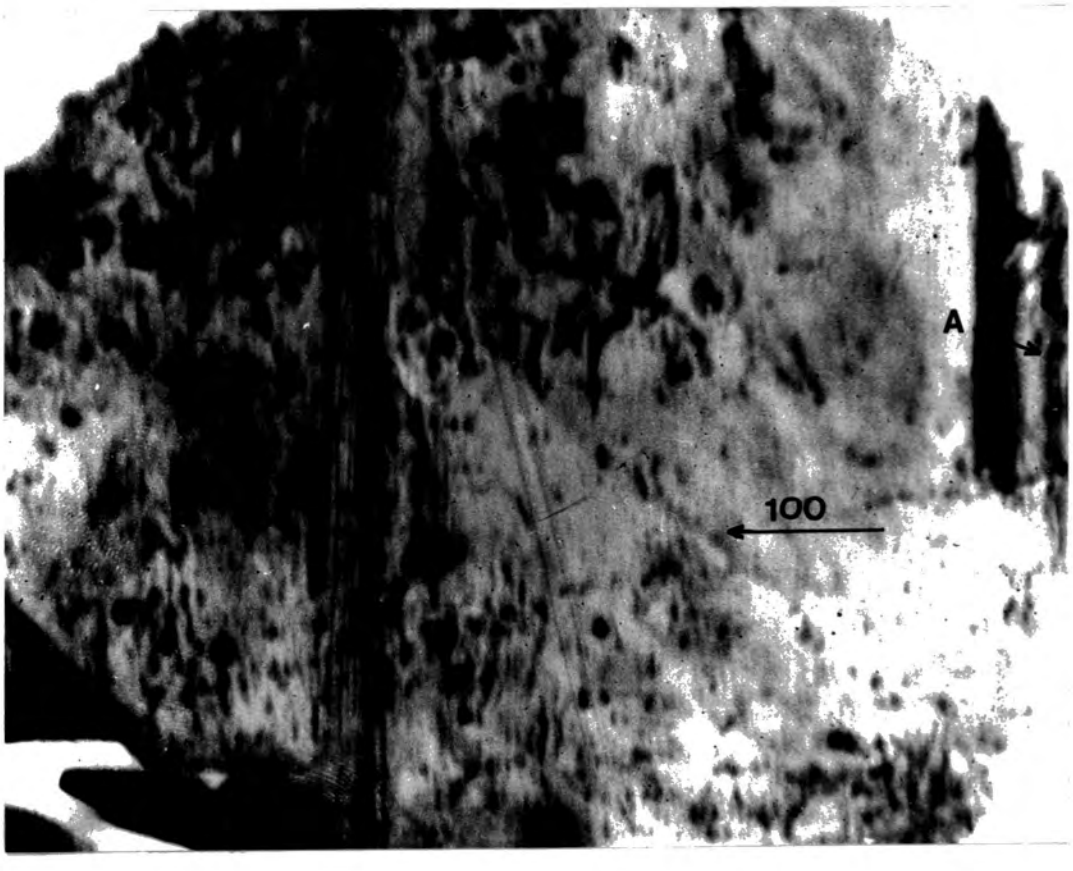

FIG 29

at A, but the bulk of the crystal appears to be single domain.

3.6 Conclusion

It can be seen that the particular properties of synchrotron radiation as outlined in the last chapter make the design and use of cryostats for X-ray topography very straightforward in contrast to those required for Lang topography. This simplicity can make fairly easy what could otherwise be rather long and difficult experiments.

4. Observation of Ferromagnetic Domains in a Terbium Single Crystal Using Synchrotron Radiation

4.1 Introduction

Terbium is a member of the heavy rare earth group having an antiferromagnetic phase between 229°K and 222°K and a ferromagnetic phase below 222°K. The c-axis is a hard direction so the magnetization is confined to the basal plane. Within this plane the anisotropy has six-fold symmetry favouring magnetization along the <10T0> or b axes.

Domain observations using the dry colloid technique were first reported by Corner and Al-Bassam in 1971 (29). Their sample, prepared by solid state electrolysis by Metals Research Limited, has been used in the present work.

4.2 Topography

The dry colloid technique, although simple in principle, can in practice be difficult, many unknown or uncontrollable factors hindering success. In addition it is a "one shot" method and, although evaporation may in principle be carried out in various magnetic fields, observation of wall movement of one set of domains in a changing field is not possible.

Other techniques may then be usefully considered. The possibility of using the Kerr effect and scanning electron microscopy have been investigated by other workers, but so far with rather disappointing results. Attempts have been made to use Lang topography on gadolinium but the rapid tarnishing of the surface coupled with the rather long exposure time cause great problems and results were once again disappointing.

This problem of tarnishing has been overcome by making use of the very much reduced exposure time made possible by using a synchrotron radiation X-ray source. In addition, distortions of the crystal lattice, which can cause problems in Lang topography of metal crystals are of less importance when a continuous spectrum is used. The success of the technique depends on the magnetostriction being sufficiently large to cause domain contrast despite the contrast produced by the bending of the lattice. This is the case for terbium ($\lambda = 3 \times 10^{-3}$ at $200^{\circ}K$).

In our experiments the crystal was polished in an acetic acid/methanol mixture and mounted with wax on the specimen holder of the glass cold finger cryostat described in section 3.2. Room temperature topographs produced with a specimen to plate distance of 15 cm. were diffuse and featureless. On cooling to about $120^{\circ}K$ the image became

even more diffuse and no domain structure could be observed. This observation is in agreement with those of Corner and Al-Bassam and is presumably a result of differential thermal strains in the crystal. When the crystal was allowed to warm to a temperature just below 222°K these strains decreased and the domain pattern shown in figure 30 was obtained. A section of this picture with further enlargement is shown in figure 31.

4.3 Discussion

The lines observed are perpendicular to the c-axis and may be interpreted as arising from parallel sheet domains lying in the basal plane. The curvature of the domain walls is interpreted as arising from curvature of the lattice planes. The spacing of the closest visible lines is about 2 μm.

Corner and Al-Bassam observed similar striped images on both the a and the b faces and from the appearance concluded that the magnetization may lie along two of the b axes but not along that b - axis perpendicular to a surface (that shown in figure 30). On the basis of this model they calculated the equilibrium domain width Do as

FIG 30

FIG 31

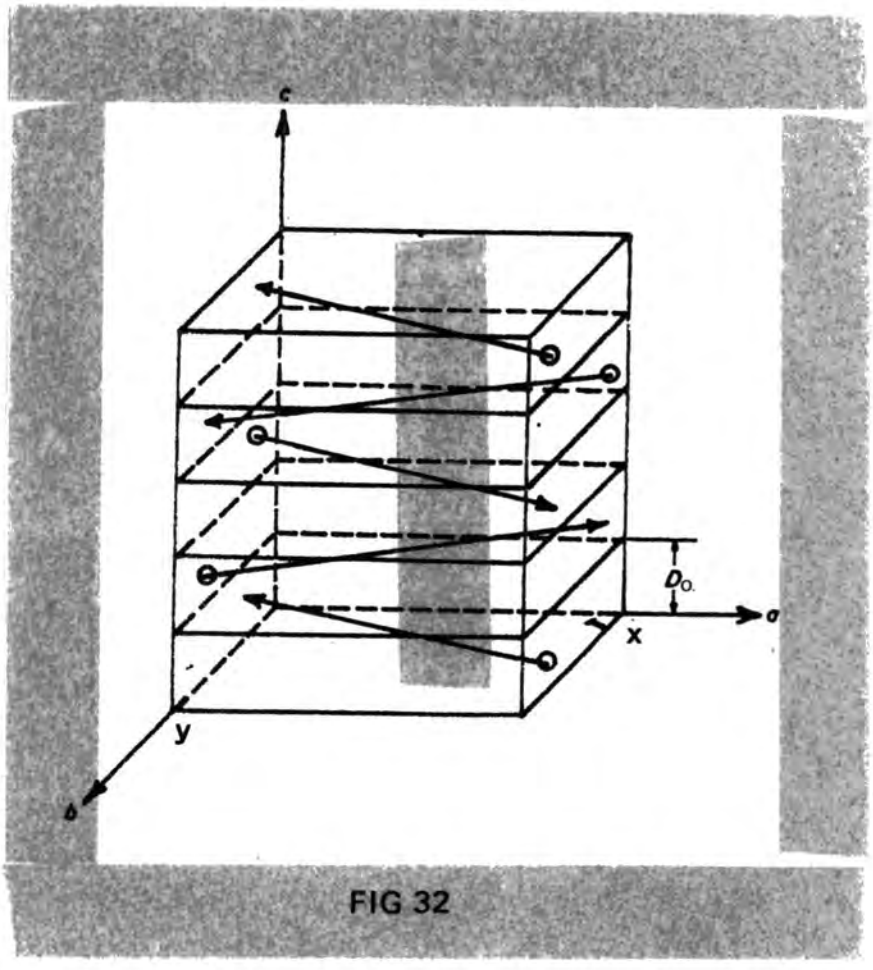

FIG 32

$$Do = \frac{2}{I_s}\left[\frac{xy\left(\frac{2KTc}{a_o}\right)^{\frac{1}{2}} K_4^{\frac{1}{2}}}{1.7\ (x + 3y)}\right]^{\frac{1}{2}} \qquad 1$$

and the minimum energy per unit volume as

$$Eo = 2Is\left[\frac{1.7\ (x + 3y)\left(\frac{2KTC}{a_o}\right)^{\frac{1}{2}} K_4^{\frac{1}{2}}}{xy}\right]^{\frac{1}{2}} \qquad 2$$

where x, y are the domain dimensions as shown in figure 32, a_o is the lattice parameter (3.6×10^{-8} cm.), K_4 is the basal plane anisotropy constant (0.18×10^6 erg cm^{-3} at 210°K) and I_s is the saturation magnetization (1556 emu cm^{-3} at 210°K). The sample was irregular in shape after polishing but the dimensions x and y may be taken approximately as 0.25 cm. and 0.30 cm. respectively. Substitution of these values into equ. 1 yields the equilibrium domain width as approximately 2 μm which is equal to the smallest line separation on the synchrotron topographs. Impurities of oxide may be responsible for the broader lines. Eo is in the order of 10^4 erg $cm.^{-3}$.

5 A Assessment of Rare Earth Aluminate and $DyFeO_3$ Crystals Grown with a MoO_3 Additive to the Flux

5 A.1 Introduction

Rare earth aluminates (R = Eu to Er) and $DyFeO_3$ have interesting magnetic properties. In particular $DyAlO_3$ and $TbAlO_3$ are magnetoelectric (Hornreich (30)) and also have antiferromagnetic phases (Cashion et al (31)). Before the growth by Mrs. B. M. Wanklyn of the crystals studied here the quality of rare earth aluminate crystals had been rather poor. The growth from flux is made difficult because, as the radius of the rare earth ion decreases, the garnet $R_3Al_5O_{12}$ tends to be formed in preference to the aluminate. The basic flux is PbO/PbF_2 and when a large amount of PbF_2 is present rare earth oxyfluoride is produced in addition to the garnet, this occuring particularly at low temperatures. Methods used to avoid these difficulties include:

(i) Using a high PbO/PbF_2 ratio.

(ii) Using a flux richer in PbF_2 but maintaining a high temperature until the concentration of PbF_2 has been reduced by evaporation.

(iii) Using R_2O_3 in excess, a measure which tends to

favour the production of the aluminate phase.

All these methods have disadvantages. A PbO rich flux leads to the nucleation of many small crystals and severely attacks the platinum of the crucible. Evaporation of the flux causes nucleation at the surface of the melt, generally producing poor results. Excess R_2O_3 is initially favourable to the growth of ROF or R_2O_3 and this tends to interfere with the production of good quality aluminates. The addition of B_2O_3 has for some time been used to improve the quality of flux grown crystals. This proved to be useful for the growth of the aluminates but an additional improvement was gained using an additive of MoO_3. This had previously been used by Wanklyn et al (32) in the flux growth of rare earth silicates and aluminosilicates, the effect being apparently to reduce the number of nucleations occuring. Details of the growth conditions are given in table (1) and more extensively in the paper by Wanklyn, Midgley and Tanner (33).

5 A.2 Assessment of Crystal Perfection

The crystals which nucleated below the melt surface appeared either plate-like or nearly cubic. The faces were optically flat and, in some crystals, growth bands were visible due to changes in refractive index. These are attributable to

Crystal	Initial Composition	Soak Temperature and Time (hrs)	Rate of Cooling (°K/hr)	Topograph
$ErAlO_3$	10.7g Er_2O_3, 2.7g Al_2O_3, 91.2g PbO, 8g PbO_2, 16g PbF_2, 4.8g MoO_3, 1.6g B_2O_3.	1290,24	1, 6 days 1.1, 3 days 1.3 to 900°C	Fig. 33
$TbAlO_3$	15.9g Tb_4O_7, 4g Al_2O_3, 140g PbO, 12g PbO_2, 45g PbF_2 2.3g B_2O_3	1295,14	1, 4 days 1.4, 4 days 2 to 900°C	Fig. 34
$TbAlO_3$	15.9g Tb_4O_7, 4g Al_2O_3, 140g PbO, 12g PbO_2, 45g PbF_2 2.3g B_2O_3, 6.8g MoO_3.	1295,14	1, 4 days 1.2, 3 days 1.5, 3 days 2 to 900°C	Fig. 35
$DyFeO_3$	2.1g Dy_2O_3, 0.9g Fe_2O_3, 6.6g PbO, 5.6g PbF_2, 0.2g B_2O_3; 0.5g PbO_2, 0.4g MoO_3	1245,17	1, 4 days 1.5, 3 days 1.9 to 900°C	Fig. 37

Table 1

slight changes in composition which may be produced by thermal fluctuations during growth. The banding indicated that the nearly cubic crystals were nucleated at the centre of a face, whereas the plate-like crystals were mostly nucleated at a corner.

The plate crystals ranged in thickness between 200 μm. and 1 mm. giving values of μt for MoKα radiation between 5 and 20. For nearly perfect crystals this is in the range of anomalous transmission and the mere existance of anomalous transmission in the plate-like crystals was an indication of their high quality. After thinning transmission was also obtained through the nearly cubic crystals although, difficulty in finding a suitable chemical polish to remove the strained surface layer produced by mechanical polishing, prevented the production of any good quality topographs. All of the topographs shown were taken using MoKα radiation and Ilford L4 nuclear emulsion.

Figure 33 is a topograph of an $ErAlO_3$ crystal. The two pairs of long straight dislocations marked D were probably nucleated by aggregrates of impurities. These impurities may adhere to the crystal during thermal fluctuations and the fact that fluctuations occured is indicated by the growth banding, this being a striking feature of the

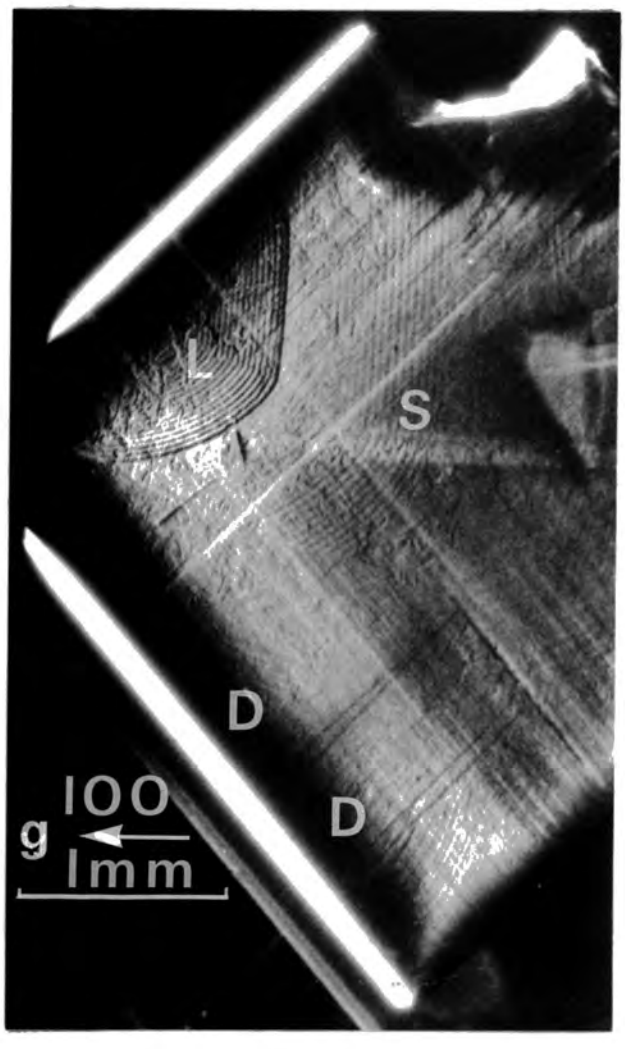

FIG 33

topograph. The crystal was nucleated at a corner and the two growth fronts are separated by a "growth sector boundary" marked S. The dislocations occur on only one side of the boundary but there is no imbalance of growth between the two sides. Some layer growth appears to have occured at L, a feature which is clearly visible optically. The appearance of this topograph, particularly as regards the dislocations is similar to crystals produced by aqueous solution growth and is very important as it is the first example of a flux grown crystal having this appearance. The importance of this as a step toward an extension and unification of the theory of crystal growth mechanisms will be considered in the next section.

The topograph of the large crystal of $TbAlO_3$ shown in figure 34 appears to be free of growth banding. This crystal grew on the surface of the melt and, despite our earlier comment on the general poor optical quality of such crystals, was in fact the best rare earth aluminate produced. No anomolous transmission occurs around the edge of the crystal, this probably being due to a distortion of the lattice by flux inclusions on the surface. This seems to be a common occurence in flux grown crystals.

The intense white bands in the photograph are produced by reflection from the edges of the crystal and so are surface reflection rather than a transmission images. In cases

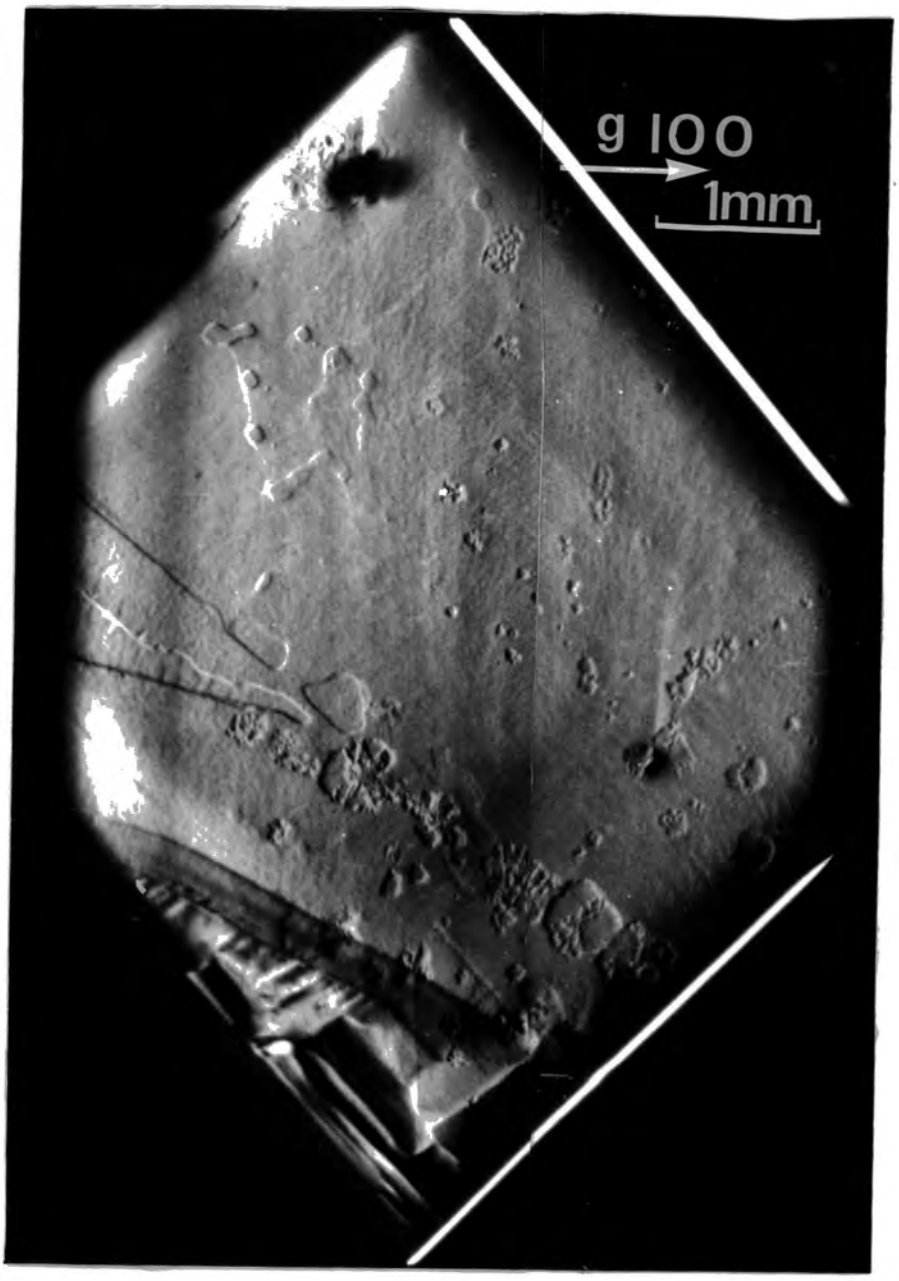

FIG 34

where the anomolous transmission is very low these intense reflections are extremely useful in setting up the crystal. Once the edge reflection has been found the crystal may be traversed to a position where an edge is not exposed directly to the incident beam. In this position the final adjustment on the weak anomalously transmitted peak may be made.

Figure 35a is a polarized light micrograph of a smaller crystal of $TbAlO_3$. Although optically this appears to be free from banding the topographs 35b and 35c do show banding. It is perhaps worth pointing out that bands similar to those in figure 35c could be produced by irregularities in the Lang camera traverse mechanism. However the fact that in figure 35b the bands are at 45° to the diffraction vector shows that banding is a true feature of this crystal. Growth appears to have only occured along the (100) edge. The sets of dislocations p and d show dynamical constrast. Dislocation d is totally absent in the $\bar{1}00$ reflection and was also absent in the $10\bar{1}$ reflection (Not shown). Thus d is a pure edge dislocation with a Burger's vector parallel to the (010) direction. The double line dislocation contrast visible in figure 35b arises from diffraction by the strain field on either side of the dislocation core. The criterion for this to occur is usually taken as $|\underline{g}.\underline{b}| \geq 2$ where $\underline{b}$ is the Burger's vector. Thus a Burger's vector of 2[010] is indicated for d.

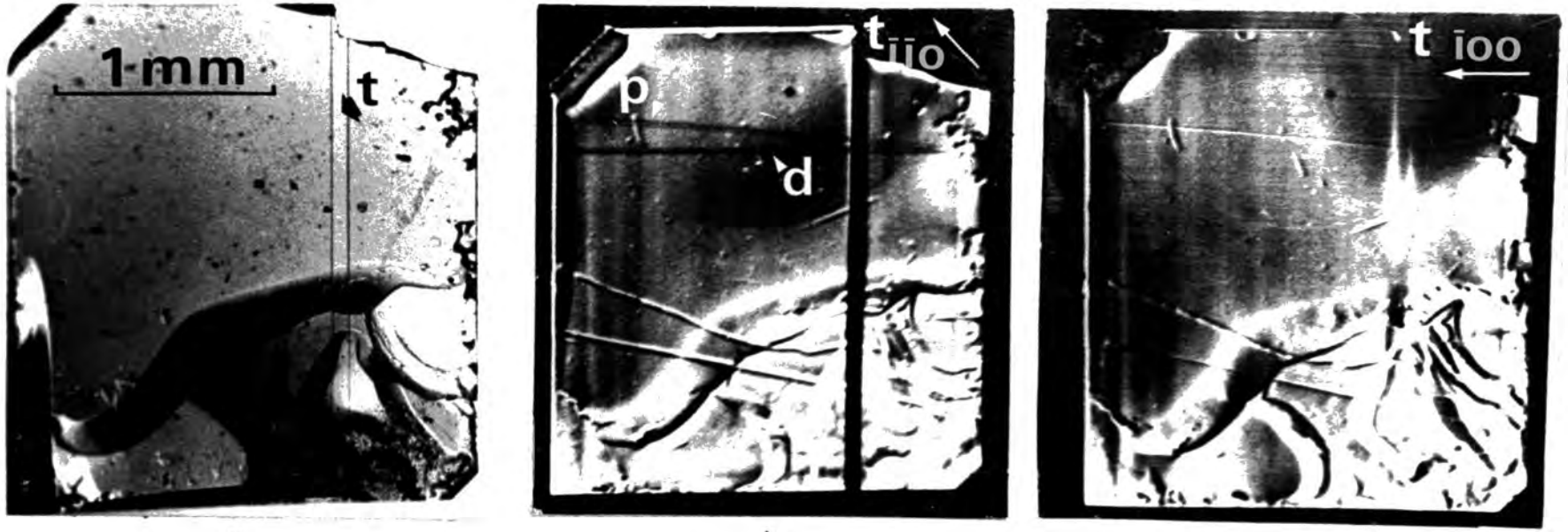

FIG 35

(The smallest value possible is taken on energy grounds.) No reflection was found for which the dislocation p disappeared although the double contrast in the $\bar{1}10$ reflection indicates a possible Burger's vector of $\pm$ [110]. If this is the case p should vanish in the $i\bar{1}0$ reflection (not shown) although in fact both p and d show enhanced diffracted intensity. This contrast was very diffuse and broad and may well arise from the residual contrast from the edge component of the Burger's vector. Once again a discussion of the importance of these observations will be given in the next section.

The polarized light micrograph has a region t, of contrast different from that of the bulk of the specimen, separated from it by two dark lines. This region did not satisfy the Bragg condition at the same time as the bulk for most reflections (e.g. figure 35b) but did so for the $\bar{1}00$ (figure 35c). Thus the region appears to be twinned with displacement vector parallel to the (010) direction. $TbAlO_3$ has a monoclinically distorted perovskite cell and twinning may occur by the interchange of the a and the a' axis as is shown in figure 36.

Figure 37 is a topograph of a $DyFeO_3$ crystal grown with MoO_3 as an additive to the flux. It was found possible to grow $DyFeO_3$ with less loss of weight from the crucible than in the growth of the aluminates, and thus the growth of $DyFeO_3$, with and without MoO_3 gives a more reliable measure

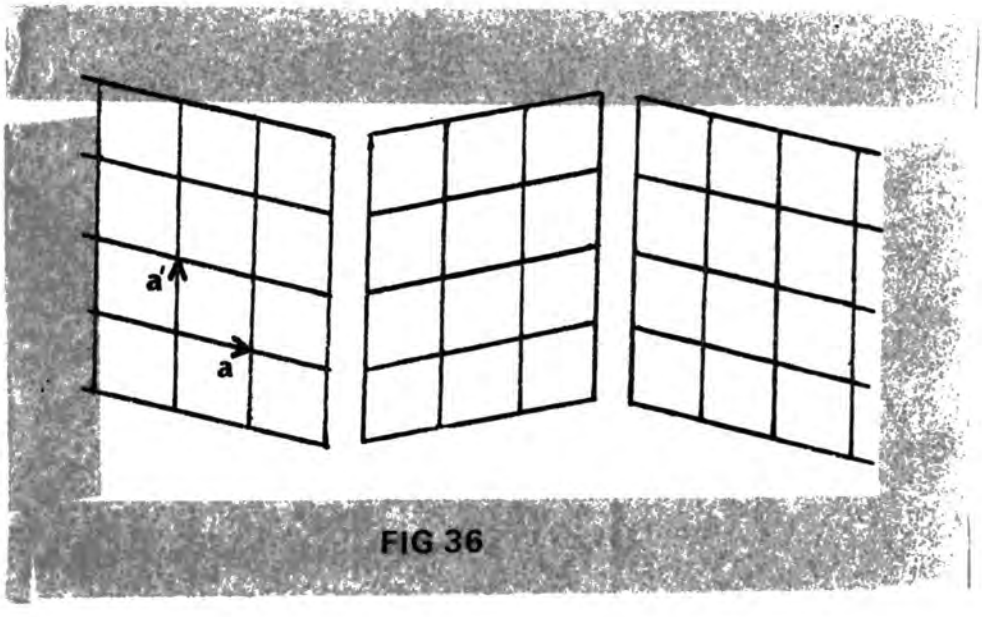

FIG 36

FIG 37

of the effectiveness of this additive in improving crystal quality. Some layer growth and growth banding is visible but no dislocations. The perfection appears to be comparable with that of the aluminates.

5 A.3 Discussion

For the number of crystals nucleated to be reduced and the growth of existing crystals to be encouraged the super-saturation for growth on an existing crystal must be less than that for nucleation. It may be possible that, since a dislocation growth mechanism seems unlikely, the effect of such additives as B_2O_3 and MoO_3 may be either to facilitate corner or edge nucleation thus encouraging layer growth across the face or to suppress the nucleation of new crystals. Other mechanisms which have been suggested to account for the effect of B_2O_3 include.

(i) reduction in flux evaporation
(ii) increase in flux viscosity
(iii) bringing undesolved particles into solution

It has been shown recently by Coe and Elwell (34) that in PbO-PbF_2 melts the viscosity and temperature are only slightly affected by small additions of B_2O_3 and this is likely to be true of MoO_3 although further work must be

done to ellucidate this point.

It was mentioned in the last section that the dislocations were of importance because of the similarity to dislocations observed in aqueous solution growth and this may be important from a theoretical point of view. The dislocations in crystals grown from aqueous solution are usually straight and do not always lie in crystallographic directions (Ikeno, Maruyama and Kato (35), Duckett and Lang (36)). Assuming a crystal grows in such a way as to minimize the free energy each dislocation prefers to be in such a direction as to minimize the elastic energy per unit of length grown. For this direction no force is exerted on the dislocation by the growth surface of the crystal (Klapper (37), (38)). In crystals of low elastic anisotropy this condition favours a direction nearly normal to the growth face but marked deviation may occur in crystals of high elastic anisotropy. In studies on crystals grown from aqueous solution preferred dislocation line directions calculated from the conditions of minimization of line energy have been compared with experimental observations, producing very good agreement. (Klapper (39), (40), (41), (42), Klapper and Küppers (43), (44), Klapper, Fishman and Lutsau (45)). Thus the fact that flux grown crystals may also have long straight dislocations lying neither exactly in a crystallographic direction nor exactly normal to the growth front leads one to expect that the same energy minimization criterion may be used for flux grown crystals as for those grown from aqueous solution.

Unfortunately the elastic constants of $RAlO_3$ have yet to be measured so a numerical test is not possible. However recently Safa et al (46) have studied the dislocation line directions in flux grown $KNiF_3$ and $KCoF_3$ and the quantitative agreement with those predicted is generally excellent. Three general rules have been formulated by Klapper and Kuppers (43) (44). Taking $\hat{n}$ as a unit vector normal to the growth front these are

(i) For a Burger's vector $\underline{b}$ parallel to $\hat{n}$, the dislocation line direction $\underline{L}$ is parallel to $\hat{n}$ (screw dislocation).

(ii) For $\underline{b}$ normal to $\hat{n}$ and $\hat{n}$ parallel to a direction of two fold symmetry $\underline{L}$ is parallel to $\hat{n}$ (edge dislocation).

(iii) For $\underline{b}$ neither parallel nor normal to $\hat{n}$, $\underline{L}$ lies between $\hat{n}$ and $\underline{b}$ (mixed dislocation).

On the topograph of $ErAlO_3$ (figure 33) two of the dislocations appear nearly parallel to each other and normal to the growth front indicating either pure screw or pure edge dislocation. The other pair although it is not particularly clear in this topograph emerge at the edge of the crystal almost parallel and normal to the growth front despite the initial divergence and may well have opposite Burger's vectors (since they originate from the same point this would

produce a null vector at that point). The dislocation d in figure 35 is as already mentioned, pure edge and obeys Klapper and Kupper's rule 2, being normal to the growth front. The dislocation p appears to be mixed and, if $b = \pm [110]$ is a correct assignment, obeys rule 3. This should make a useful quantitative test of the theory when the elastic constants become available.

5 B Assessment of Rare Earth Arsenates Produced both with and without Hot Pouring

5 B.I Introduction

The rare earth arsenates $RAsO_4$ (R = Sm to Lu) have the tetragonal zircon structure ($ZrSiO_4$). At low temperatures the arsenates with R = Gd,Tb,Dy have antiferromagnetic phases and those with R = Tb, Dy, Tm have Jahn-Teller transitions. The growth of rare earth arsenates has been reported before by Fiegelson (47) but only needle shaped crystals were produced. Rare earth vanadates and phosphates have been grown from $Pb_2V_2O_7$ and $Pb_2P_2O_7$ fluxes by slow cooling (Smith and Wanklyn (48)) and it was proposed to produce RA_sO_4 in the same way. This, however, presented several problems. $Pb_2As_2O_7$ is very toxic and much more volatile than $Pb_2V_2O_7$ or $Pb_2P_2O_7$, thus necessitating the protection of the furnace from contamination and the provision of good ventilation. In addition to these problems the arsenates are brittle and tend to fracture as the flux contracts around them. Thus a facility for hot pouring of the flux was desirable to separate the flux and crystals before the flux solidified. The remainder of this chapter is devoted to the growth and comparison of rare earth arsenates produced both with and without hot pouring.

The apparatus used by Dr. S. H. Smith at the Clarendon Laboratory Oxford is illustrated in figure 38. A tube of sillimanite (1 m. long and 14 cm. in diameter) is supported at each end by a pair of wheels mounted on a scissor jack. The tube passes through a rectangular furnace between arrays of heating elements, the ends of the chamber being blocked with alumina brick plugs leaving clearance enough for rotation of the tube about it's axis. In a typical experiment two pure platinum crucibles were placed one above the other in an alumina crucible, the space around them being filled with MgO powder. A layer of $CaCO_3$ powder was added before fitting an alumina lid. The MgO and $CaCO_3$ powders react with vapours or liquid flux which may escape from the crucibles. Usually two alumina crucibles were used in each experiment. At the desired point in the heating cycle the crucibles could be inverted by rotation of the sillimanite tube leaving the crystals attached around the base of the platinum crucibles and thus separated from the molten flux. Details of the growth of the specimens examined here are given in table 2.

5 B.2 Assessment of Crystal Perfection

Optically clear rods up to 10 mm x 2 mm x 2 mm and plates up to 5 mm x 4 mm x 0.2 mm were obtained. Topographs were taken of several of the as-grown crystals using $AgK\alpha$, radiation and Ilford L4 nuclear emulsions. Once again the

Crystal	Initial Composition	Growth Programme	Hot-poured?	Topograph
$TmAsO_4$	2.5 wt% Tm_2O_3 in 23g flux	1350°C to below 800°C at 1°K/hr	No	Fig. 39
$DyAsO_4$	2.5 wt% Dy_2O_3 in 23g flux	1380°C to about 860°C at 1°K/hr	No	Fig. 41
$DyAsO_4$	2.5 wt% Dy_2O_3 in 23g flux	1380°C to 1080°C at 1°K/hr	Yes	Fig. 42
$Lu_{0.98}Tm_{0.02}AsO_4$	3.5 wt% R_2O_3 in 68g flux	1400°C to 1290°C and then 1300°C to 1050°C, both at 1°K/hr	Yes	Fig.43

Table 2

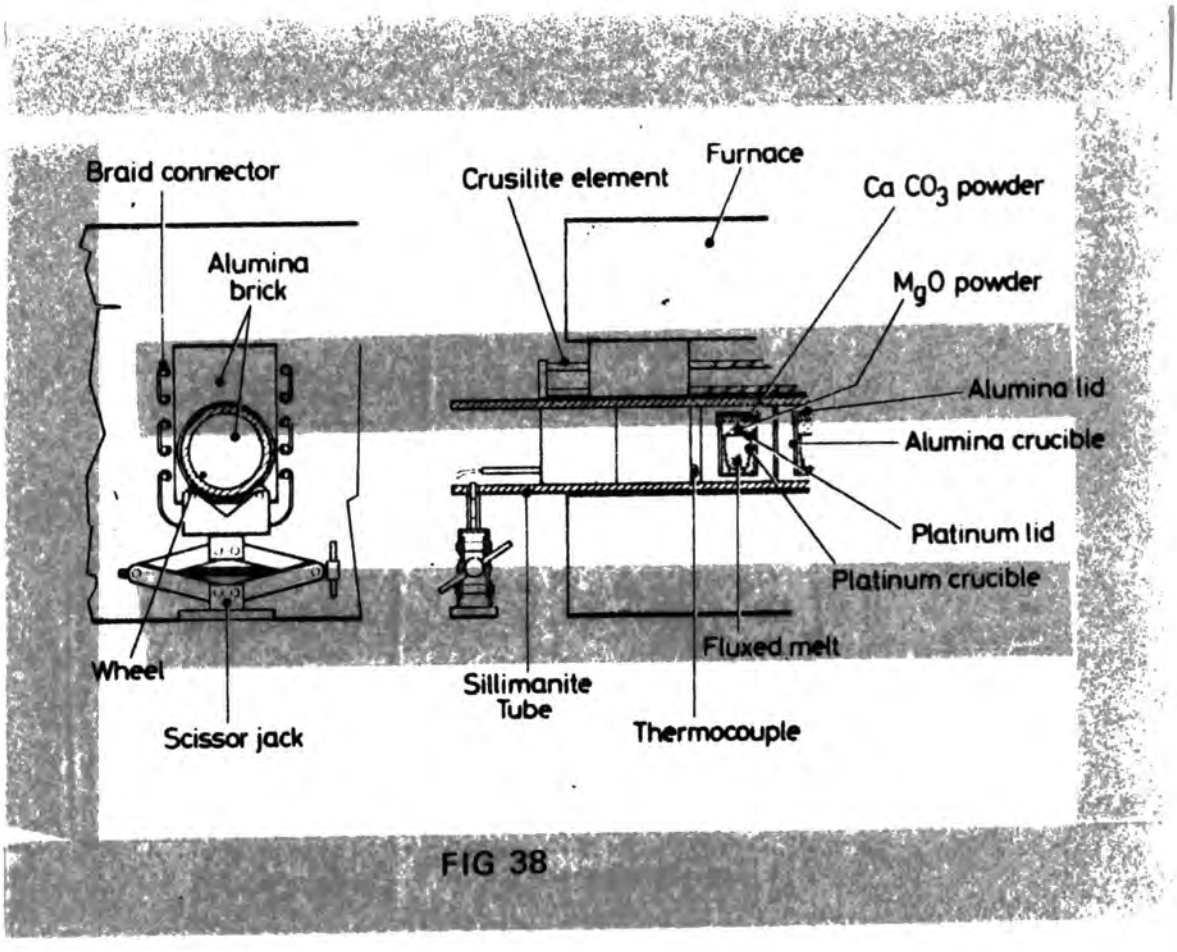
Braid connector
Crusilite element
Furnace
Ca CO_3 powder
Alumina brick
M_gO powder
Alumina lid
Alumina crucible
Platinum lid
Platinum crucible
Fluxed melt
Wheel
Sillimanite Tube
Thermocouple
Scissor jack

FIG 38

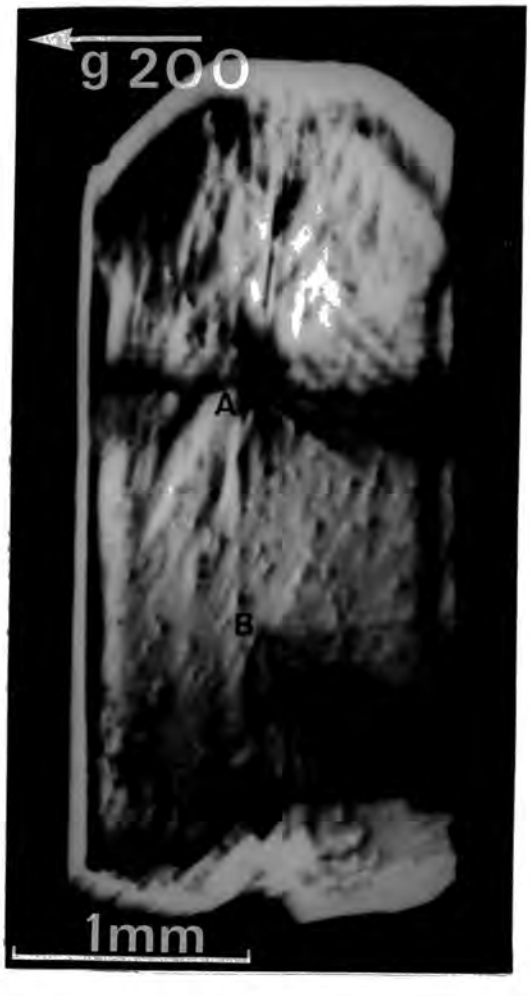
g 200
A
B
1mm

FIG 39

very existance of anomalous transmission was an indication of high crystal perfection.

The topograph of $TmAsO_4$ shown in figure 39 shows dislocations radiating from points A and B, these probably being nucleated by flux inclusions. This crystal was recovered from below the surface of the melt in one of the earliest experiments where hot pouring was not attempted and, despite the dislocations seems to have large perfect areas. The only defects visible in these regions are precipitates showing black-white contrast, typical of defects lying close to the surface. The reasons for this may be seen in figure 40 which shows the lattice curvature around a precipitate lying close to the surface. As the wave field propogates through the crystal tie point migration occurs up to a point at X below the exit surface where the curvature becomes so large that no further diffraction is possible. Qualitative consideration of the dispersion surface then leads one to expect that for the diffraction vector shown enhanced intensity will be produced by the right hand side of the precipitate strain field and diminished intensity by the left. This fits the observations well so we may conclude that the images on the topograph are produced by defects of this type compressing the surrounding lattice.

The topograph of the $DyAsO_4$ crystal shown in figure 41 illustrates the importance of controlled cooling conditions.

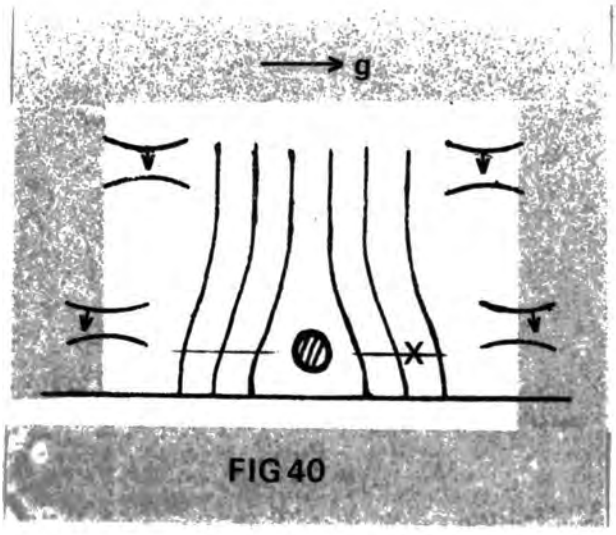

FIG 40

FIG 41

The erratic conditions which occured during the growth of this crystal appear to have produced many inclusions and many long straight dislocations parallel to the c-axis. Polishing failed to remove the damage. Such dislocations did not appear in topographs of crystals grown under steady cooling conditions.

Figure 42 is of a topograph of hot poured $DyAsO_4$ and is typical of crystals produced by hot pouring. The surface is covered with precipitates, many more than on crystals which were not hot-poured. This effect is attributed to drops of flux remaining on the surface after hot pouring. No other defects are visible. The precipitates were difficult to remove and prolonged boiling in concentrated nitric acid had little effect. Mechanical polishing on a diamond wheel followed by chemical etching did remove the precipitatesthus confirming that they were near the surface but the surface was left in a badly damaged condition and the topographs were rather poor. However no bulk defects could be identified and we believe the crystal to be of good quality.

The crystal of the mixed arsenate $Lu_{0.98}Tm_{0.02}AsO_4$ a topograph of which is shown in figure 43, was grown in a crucible with a welded lid and was hot poured. The loss of flux by evaporation was thus very low. The quality is probably no better than that of the hot poured $DyAsO_4$,

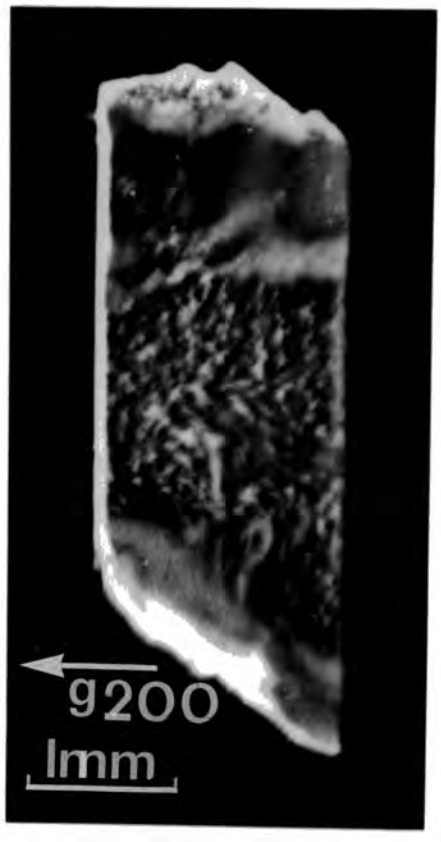

FIG 42

FIG 43

and thus it appears that the perfection may not be significantly reduced by flux evaporation. Small positive steps were included in the cooling. These did not appear to affect the crystal quality either and it may be possible in this manner to control the number of nucleations and hence the size of the crystals produced.

5 B.3 Conclusion

Large good quality crystals of $RAsO_4$ may be produced by slow cooling from a $Pb_2As_2O_7$ flux but the risk of fracture or plastic deformation during flux solidification makes hot pouring a useful alternative. Hot pouring does, however, introduce surface precipitates and some further investigation is needed to remove these and leave an undamaged surface.

6 Observation of Jahn-Teller Domains in Dysprosium Vanadate.

6.1 Introduction

The co-operative Jahn- Teller effect is a phase transition produced by an interaction between the crystal lattice and orbital electrons involving a splitting of degenerate electron states and a distortion of the lattice which lowers the crystal symmetry. The theoretical interpretation involves a correction to the familiar Born-Oppenheimer approximation which has been a basic concept in much of our understanding of the electronic properties of solids. This approximation is that the motion of electrons in unfilled shells is so rapid that it may be considered to be independent of the motion of the nuclei i.e. the motion of these electrons is treated as being relative to a static lattice. In certain high symmetry atomic sites orbital degeneracy may occur and in such situations the Born-Oppenheimer approximation may become invalid. Englman (49) gives a detailed account of the theory. In such cases pure electronic and vibrational modes do not exist and the term vibronic has been coined to describe the mixed modes which occur. The basic mechanism for the Jahn-Teller effect is that small displacements of ions surrounding the Jahn-Teller active ion can alter the crystal field acting on that ion. The surrounding ions act upon each other through elastic interaction and so this produces an effective interaction between

the Jahn-Teller ions. If the Jahn-Teller ion concentration is sufficiently high the entire crystal may be unstable under some distortion. It is possible for different distortion directions to occur in different parts of the crystal, thus forming domains. In practice the choice of distortion direction will depend on the existance of local strains in the crystal.

Research into the Jahn-Teller effect has been stimulated during the past eight years due in part to the realization by Allen (50) and Pytte (51) of the importance of elastic constant measurements through the phase transition and the subsequent use of ultrasonic techniques and in part to the growth of a family of transparent rare earth crystals, some of which exhibit the Jahn-Teller effect, in which the transparency allows the use of optical techniques to investigate changes in electronic energy levels.

It is this family of crystals, the rare earth zircons (RVO_4, RPO_4 and $RAsO_4$) with the Jahn-Teller active rare earth ion, which concerns us here, in particular dysprosium vanadate. The transitions to the Jahn-Teller distorted phase occur at low temperatures, a fact which confers the advantage to observations of such things as spectral lines and specific heat anomalies that masking by thermal effects is limited. This is not an advantage in X-ray topography where the techniques of mounting crystals strain free which

are used at room temperature may prove inadequate when the temperature is reduced. A comprehensive discussion of theoretical and experimental investigations into the Jahn-Teller effect in solids with particular reference to the rare earth zircons has been given in a recent review article by Gehring and Gehring (52). This article gives an exhaustive list of references.

6.2 Observation of the Jahn-Teller effect in Dysprosium Vanadate

In 1970 Cooke et al (53) reported the results of low temperature spectroscopic, specific heat and magnetic moment measurements on $DyVO_4$. From their observations they concluded that at about 14^oK a Jahn-Teller distortion occurs in which the crystal symmetry is lowered from tetragonal to a probable orthorhombic phase. The orthorhombic symmetry of the phase below 14^oK was subsequently confirmed by Becker and Laugsch (54). (An antiferromagnetic ordering occurs at about 3.1^oK but no crystallographic change has been observed.) Sayetat et al (55) have performed low temperature X-ray powder measurements on $DyVO_4$ and give the following data for the distortion.

Tetragonal phase	Orthorhombic phase
$a = 7.1395$ Å	$a = 7.1515$ Å
	$a' = 7.1275$ Å
$c = 6.2899$ Å	$c = 6.2899$ Å

Right from the earliest observations polarized light microscopy had revealed the existance of domain-like structures and a convincing micrograph of domains on the c-plane was produced by Gehring and Rosenberg (56). Their crystal was clamped in place by varnish to provide a good thermal contact and the strain produced by this mounting leads to very narrow domains (~1μ.m.), the strain field in this case acting in a manner analogous to the magnetic field in the case of ferromagnetic domains. The domain walls lie, as expected, along the (110) and (1$\bar{1}$0) directions.

Certain difficulties arise when contemplating X-ray topographic studies of Jahn-Teller domains in $DyVO_4$. Symmetrical reflections in the c-plane (e.g. 200) appear to be the most useful choice for producing reasonably rapid high contrast topographs. However, the domain walls lie at 45° to the entrance surface and if the domains are very narrow the incident wavefield will cross a multilayer sandwich of regions which satisfy the Bragg condition and regions which do not, where absorption will be high. Contrast

may thus be complicated.

These considerations lead to a compromise in the choice of specimen thickness. On the one hand a thin crystal may be desirable to avoid the complication of too many overlapping domains, whilst on the other a thin crystal may suffer more from deformation produced by the difference in thermal contraction of the crystal and the material used to fix the crystal to the specimen holder. For our initial experiments a specimen of about 150μm thickness was selected from a batch provided by Dr. S. H. Smith of the Clarendon Laboratory. This specimen was mounted on a brass ring using varnish and the ring held in the specimen holder of the Meric cryostat (shown mounted on the Lang camera in figure 44 with detail in figure 45) with vacuum grease. Figure 46 shows a liquid nitrogen temperature 200 reflection topograph of this specimen taken using MoKα radiation on 50μmL4 emulsion. As can be seen the surface is covered with precipitates, these proving as difficult to remove as those on the surface of the hot poured arsenates discussed in the last chapter. That these were not particularly troublesome can be seen from the topograph taken at 4.2°K shown in figure 47 in which domains are clearly visible. It was in fact easy to resolve the splitting in diffraction peaks produced as the temperature was lowered through the transition. Two regions A and B of very high diffracted intensity occur. The faint lines visible at C indicate that these broad regions do not

FIG 44

FIG 45

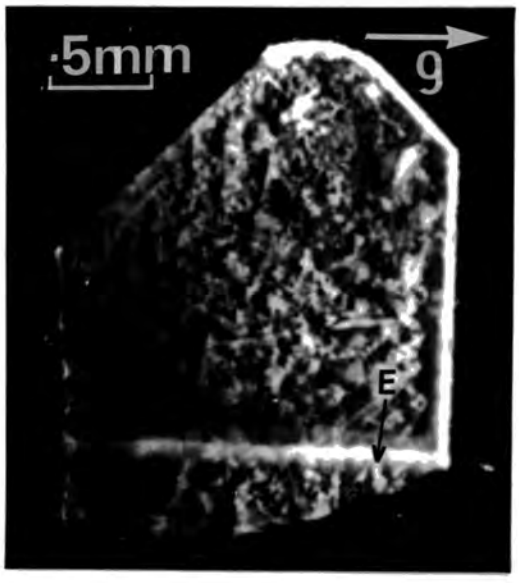

FIG 46

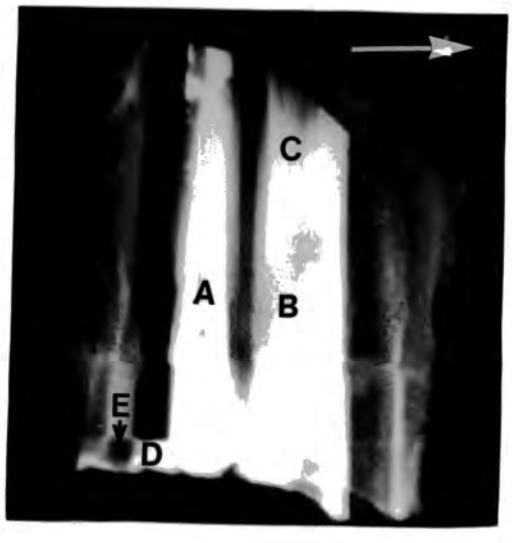

FIG 47

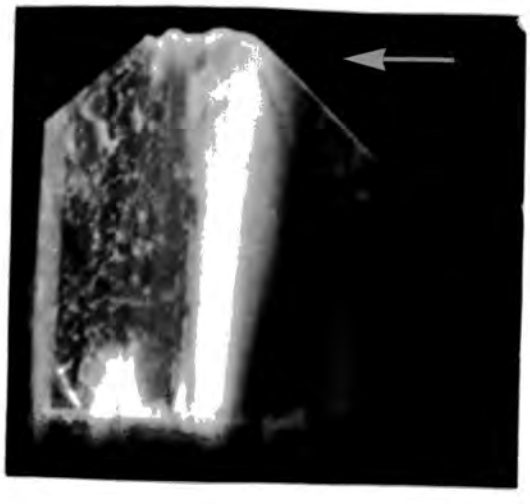

FIG 48

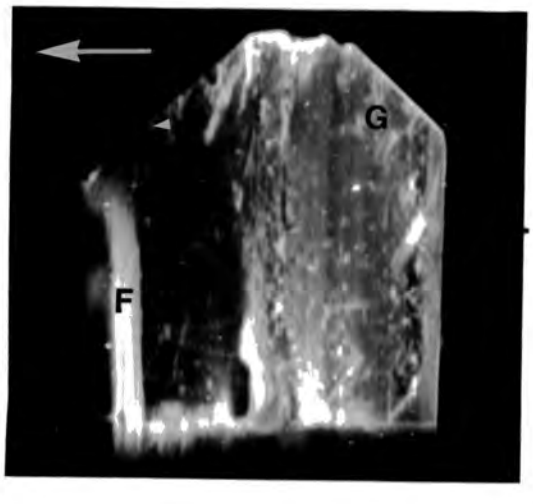

FIG 49

correspond to single domains but to many closely spaced domains. The region D is interesting in that a and a' appear to have interchanged along the c-axis, the line E which is clearly visible in figure 46 apparently forming an incoherent boundary between them. This boundary is probably a bundle of dislocations but further investigation would be necessary to determine the exact nature and how matching of the lattice across the boundary occurs. Figures 48 and 49 illustrate how sensitive the domain structure is to strain produced by the mounting of the crystal on the specimen holder, the domain structure being very irregular and no correlation being shown between individual topographs. The region F of figure 49 shows straight regularly spaced domains; the region G is however rather curious showing considerable curvature.

After these Lang topographs were produced experimental time became available on NINA and the opportunity to observe the domain structure in a magnetic field presented itself. Polarized light micrographs of Jahn-Teller domains in magnetic fields have been produced by Leask et al (57). If the field is applied along one of the distortion directions a single domain may be obtained in a certain critical field Hc. In their experiments on $DyVO_4$ at $1.6^{o}K$ (i.e. below the Neel temperature) Leask et al found Hc to be 3.7 KOe.

The set of topographs taken at room temperature shown in figure 50 comprised our first observation of a $DyVO_4$ crystal using synchrotron radiation. This is a thicker crystal ($\sim$ 0.5mm) and there appears to be no evidence, in the form of streaking in the image, of extensive straining of the lattice produced by the mounting of the crystal. Although streaking does occur quite markedly in the strong reflection labelled A, this is probably inherent in the crystal, possibly produced by the strain fields associated with the surface precipitates. Growth banding running parallel to the c-axes is apparent in most reflections of the room temperature set, excepting those from planes which are nearly perpendicular to the c-axis, showing that the distortion producing the growth bands lie in the c-plane. Dislocations nucleated at an inclusion of flux in the body of the crystal appear in all the reflections where details are discernable. Figure 51 shows the same crystal at about $4.2^{o}K$ with the Jahn-Teller distortion clearly visible. In the light of our comment on the Lang topograph of the thin crystal shown in figure 47 it is interesting that a reversal of a and a' again occurs across a boundary of dislocations. In the reflection B of figures 50 and 51 a break in the image occurs in the low temperature set at the point H which appears to coincide with the point in the room temperature set where the dislocations intersect with the edge of the crystal. It is perhaps worth pointing out that whilst the reflection A which is basically 200 might

FIG 50

FIG 5I

seem the sensible choice of reflection for investigating the domain structure, the reflection B, where the index has a non-zero component on the c-axis can actually give more information in the synchrotron case, in that the spatial origin of the contrast may be pinpointed. In this case the information on spatial origin may be slightly misleading. Lines occur which at first sight appear to be reflections from the edge of the crystal. The Lang topograph of the same crystal shown in figure 52 provides a clue to an explanation of such a large number of lines. The crystal was not remounted in the time between producing the Lang and synchrotron topographs so the strain produced by the mounting should be similar and a similar domain structure might be expected. The Lang topograph has an intense line which may result from a strain field at a point where a domain wall cuts a surface. Considering first the region to the left of the dislocation boundary the model illustrated in figure 53 gives a possible explanation of the five intense lines. The Bragg angle for reflection B is approximately 12.7^{o} and the specimen to plate distance 15 cm. Taking line 1 the reflection from the edge of the bulk of the crystal as a reference line and utilizing the values given earlier for the latticedistortion, the twinned regions **X** and **Y** would give rise to two strong edge reflections 2 and 3 at $\pm$ 1·01 mm. from 1. Lines 4 and 5 could be produced at the intersection of the twin boundaries with the entrance

FIG 52

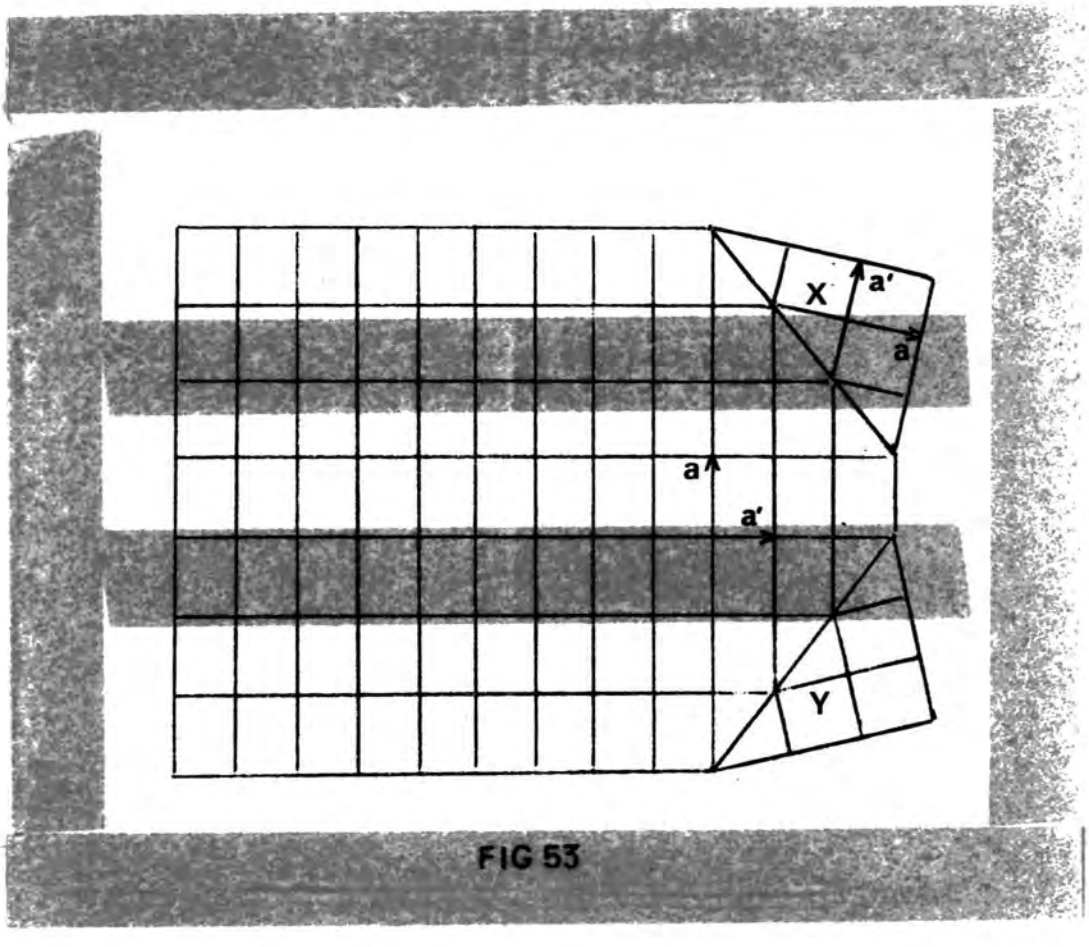

FIG 53

and exit surfaces.

Measurements from the topograph yield the distance from 1 to 2 and 3 as 1.17 mm. The spacing of lines 2 and 4 and of lines 3 and 5 indicate that if this model is valid then the twinned regions must extend at the edge to nearly half the crystal thickness. This model gives reasonable agreement with observations for the left hand side of the crystal. The right hand side is more difficult to explain and so far no convincing model has been obtained.

When further experimental time became available on NINA experiments in a magnetic field were conducted using the thinner crystal. The field was applied along the long edge perpendicular to the c-axis. The topograph shown in figure 54, taken in a field of 0.72 KOe, shows evidence of lattice curvature or variation of lattic parameter and once again a break in contrast is observed in the region of the dislocations. On increasing the field to 2.4 KOe, the domain-free image of figure 55 was obtained, this being similar to the image of the crystal above the transition temperature. On returning the field to zero the domain structure did not reappear. When the crystal was warmed above the transition temperature and then re-cooled to 4.2°K the domain structure shown in figure 56 was produced. This is quite different from that of figure 54, indicating that in this crystal the

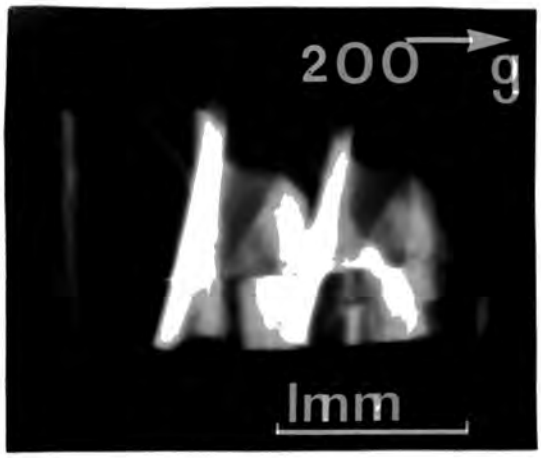

FIG 54

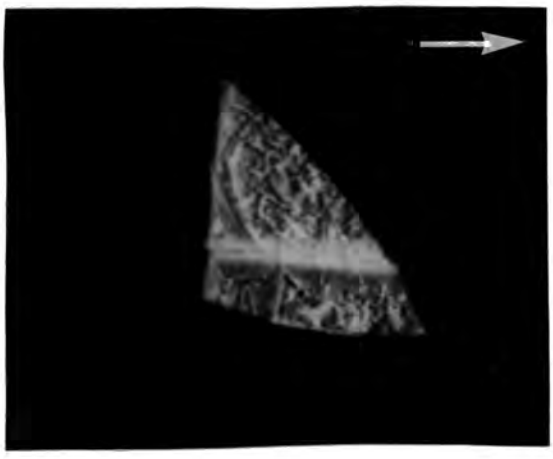

FIG 55

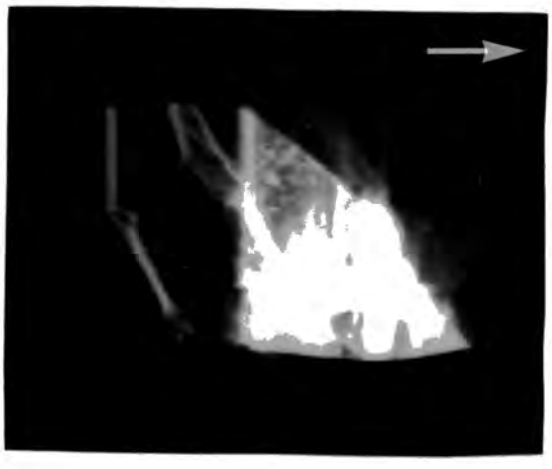

FIG 56

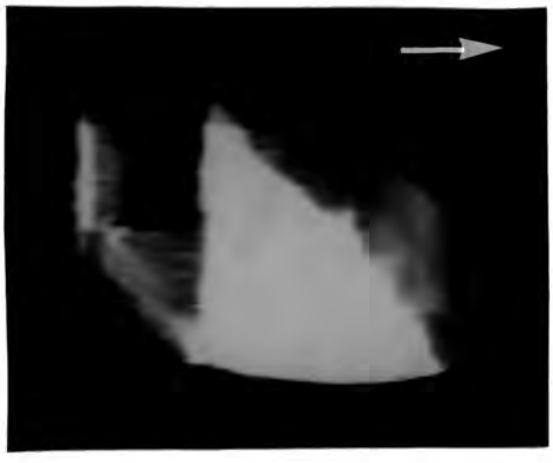

FIG 57

strain produced by the mounting dictates the domain structure. In figure 57 produced in a field of 1 KOe, the crystal appears to be on the point of becoming single domain. The next topograph (Not shown) taken in a field of 1.6 KOe had the appearance of figure 55. In both of these experimental runs the critical field was considerably less than that observed by Leask et al.

6.3 Conclusion

Both Lang and synchrotron topographs of Jahn-Teller domains in $DyVO_4$ have been produced. It is apparent that the orientation contrast inherent in synchrotron topographs can provide more information for the construction of domain models. Experiments in a magnetic field have been carried out, these indicating that a careful choice of crystal thickness is required to minimize the effects of strain and so relate the field strength to the domain structure.

7. Domain Walls and Magnetic-optics of Ferric Borate

7.1 Introduction

The work described in this chapter arose out of attempts to detect a 120° Bloch wall in the basal plane of the hexagonal, transparent, canted antiferromagnet $FeBO_3$. The anisotropy for spins lying out of the basal plane is so high that in practice the magnetization is confined to that plane. Within this 'easy plane' the anisotropy has three-fold symmetry. Lacklison, Chadwick and Page (58) have suggested a domain wall model with Bloch walls in the basal plane and Neél walls perpendicular to it. Haisma and Stacy (59) have reported the observation of optical interference fringes in a specimen of $FeBO_3$ cooled below 190°K. These they interpreted as arising from the presence of a Bloch wall which at low temperature rotates out of the basal plane. No direct evidence for the existence of this wall has been found although we do present evidence for the existence of domain walls inclined to the c-axis and the basal plane which form a closure structure.

An examination of published results on the magneto-optics of $FeBO_3$, suggested that an analysis of the effect of a Bloch wall in the basal plane on the optics of the crystal could be helpful in deciding if such a wall exists. Since the magnetization is confined to the basal plane the problem in

essence is that of analysing Faraday rotation and birefringent effects on plane polarized light incident on a platelet of $FeBO_3$ at an angle to the c-axis. The analysis, both with and without an in-plane Bloch wall which is described in the remainder of the chapter is performed for the simple case of a 180° Bloch wall using two methods, those of the Poincaré sphere and the transmission matrix. This serves both as a check on the results obtained and as a comparison of the merits of the two methods for magneto-optical calculations.

7.2 X-ray Topography of Ferric Borate

Figure 58 is a topograph of $FeBO_3$ taken with CuKα radiation on L4 50 μm. emulsion, the reflection being 110 in triply primitive hexagonal axes. Assuming that the feature A is an inclined domain wall the lines on it may be interpreted as Pendellösung fringes. The extinction distance for this reflection is about 3.0μm(Appendix) which indicates an inclination of about 4° to the surface, the same as that Haisma and Stacy give for the wall they observed at low temperature. Assuming that all features showing fringe like contrast are inclined domain walls forming a closure structure and that the normal components of magnetization are continuous across a domain wall, then the domain structure shown in figure 59 would seem to account for the main features of this topograph.

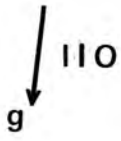

FIG 58

1mm

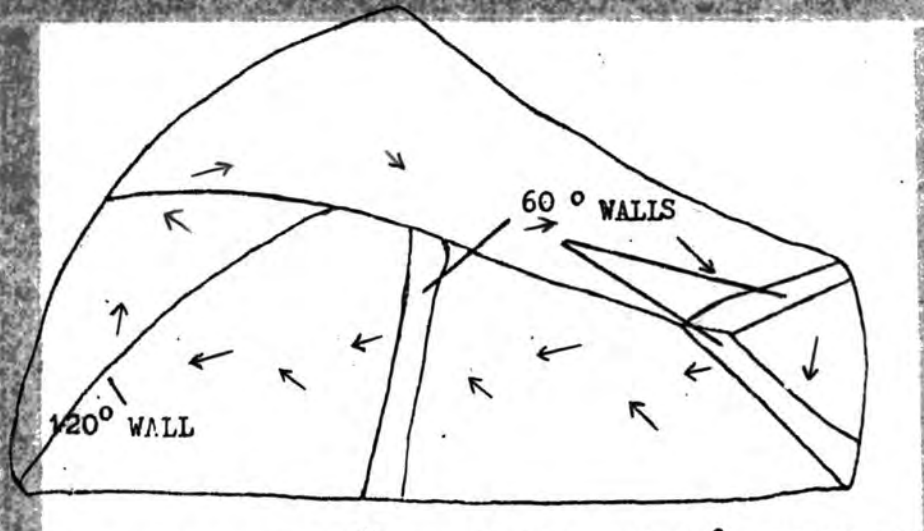

Domain model with 120° perpendicular and 60° inclined walls

FIG 59

Figure 60 is a low temperature ($\sim$120°K) topograph taken using MoKα radiation using the cryostat described in section 3.2 The extended domain wall B is also inclined at about 4° to the surface which suggests that the inclined wall observed by Haisma and Stacy may be due to an extension of the closure structure at low temperature.

7.3 The Poincaré Sphere Method

The Poincaré sphere is a construction in which points on the surface of a sphere represent the possible polarization states of an electromagnetic wave. The properties of this construction have been reviewed by Ramachandran and Ramaseshan (60) with special reference to the problem of separating birefringent and purely rotatory effects. For this section we use their notation.

The construction is illustrated in figure 61. The co-ordinate system is geometric in the most literal sense i.e. surface points are represented by a latitude and a longitude. The circle through the points C_l,V,C_r and H is the great circle of longitude 0° and 180°. The poles C_l and C_r represent left and right hand circularly polarized light and all plane polarized modes are represented by points on the equator, H standing for horizontal and V for vertical polarization. A point such as P with longitude 2λ and latitude 2ω represents elliptical polarization with the

FIG 60

1mm

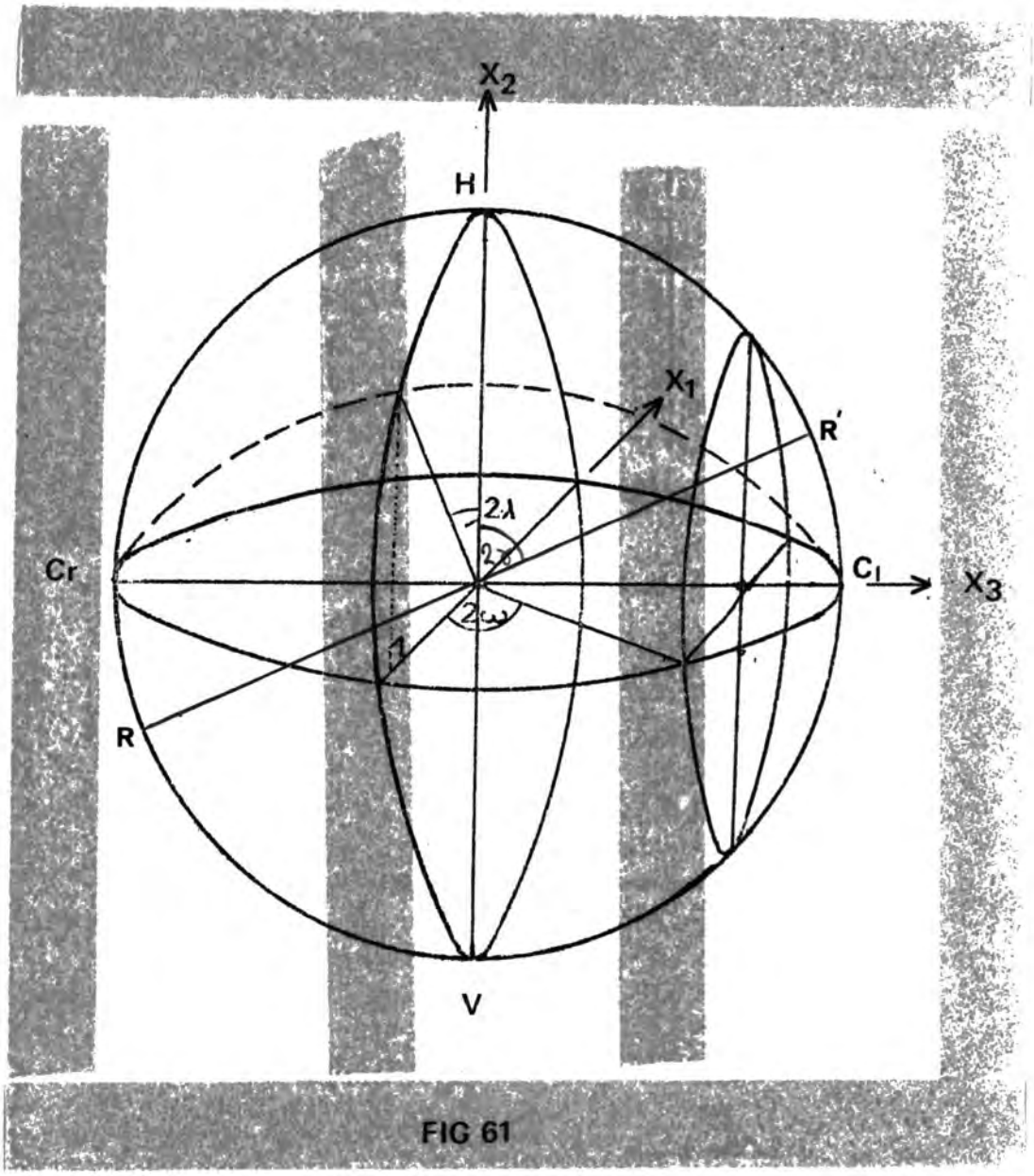

FIG 61

major axis at an angle λ to the horizontal and with the ratio of axes b/a given by

$$b/a = \tan\omega$$

ω is positive measured from the equator toward C_l. Thus all left rotating ellipses are on the hemisphere with C_l as pole and all right rotating ellipses are on the hemisphere with C_r as pole.

This then is the basic representation. We describe now further constructions on this sphere which will enable us to investigate rotating birefringent media. A line RR′ is drawn in the C_l, V, C_r, H plane at an angle 2γ to HV where

$$\tan 2\gamma = 2\varrho_o/\delta_o$$

(δ_o is the phase retardation per unit length, ϱ_o is the true rotation per unit length)

$$\text{Let} \qquad \Delta_o = (\delta_o^2 + 4\varrho_o^2)^{\frac{1}{2}}$$

Then, taking as an example P to be the initial polarization state, the state after a path length L in the medium is found by rotating P through an angle $\Delta_o L$ about RR′. The validity of this construction follows from the electromagnetic

theory of light propogation in rotating birefringent media which is described by Szivessy (61). We now turn our attention to practical cases which may exist in ferric borate.

7.3.1 The Single Domain Case

We are primarily interested in the orientation of the major axis of the emergent elliptically polarized light. This is fairly simple to find geometrically but, with the more complicated two domain case in mind, we will write the solution in terms of rotation matrices.

As previously mentioned a general state of polarization may be represented by a longitude 2λ and a latitude 2ω. Expressing these co-ordinates in a cartesian frame as shown in figure 61 we have, for a sphere of unit radius

$$\begin{aligned} x_1 &= -\cos 2\omega \sin 2\lambda \\ x_2 &= \cos 2\omega \cos 2\lambda \\ x_3 &= \sin 2\omega \end{aligned} \qquad (1)$$

To effect the rotation about RR′ we first express these coordinates in a set of axes rotated about x_1 until the transformed x_2 axis is colinear with RR′. We then rotate about this axis through an angle $\Delta = \Delta_0 L$. This is to

regarded not merely as a convenient change of axes but as a real change of coordinates within the same axes. The final step is to express these changed coordinates in the original axes. Thus we have

$$\begin{bmatrix} x_1^f \\ x_2^f \\ x_3^f \end{bmatrix} = \begin{bmatrix} 1 & 0 & 0 \\ 0 & \cos 2\gamma & \sin 2\gamma \\ 0 & -\sin 2\gamma & \cos 2\gamma \end{bmatrix} \begin{bmatrix} \cos\Delta & 0 & \sin\Delta \\ 0 & 1 & 0 \\ -\sin\Delta & 0 & \cos\Delta \end{bmatrix} \begin{bmatrix} 1 & 0 & 0 \\ 0 & \cos 2\gamma & -\sin 2\gamma \\ 0 & \sin 2\gamma & \cos 2\gamma \end{bmatrix} \begin{bmatrix} x_1 \\ x_2 \\ x_3 \end{bmatrix}$$

The final state which is in general elliptically polarized is completely described by this equation. For the simple case of incident horizontally polarized light for which $2\lambda = 2\omega = 0$ theemergent state is given by

$$\begin{bmatrix} x_1^f \\ x_2^f \\ x_3^f \end{bmatrix} = \begin{bmatrix} \sin 2\gamma \sin\Delta \\ 1 - \sin^2 2\gamma(1 - \cos\Delta) \\ \sin 2\gamma \cos 2\gamma(\cos\Delta - 1) \end{bmatrix} \qquad 2$$

The angle between the major axis and the horizontal is given from equation 1 by $\left|\frac{1}{2}\tan^{-1} x_1^f / x_2^f\right|$. Thus from equation 2 we have

$$|\lambda| = \tfrac{1}{2}\tan^{-1}\left[\frac{\sin 2\gamma \sin\Delta}{1 - \sin^2 2\gamma(1 - \cos\Delta)}\right]$$

7.3.2. The Two Domain Case

In treating the two domain case we assume that the Bloch wall is thin compared with the domain thickness so that optical effects in the wall may be neglected. The solution is thus simply an extension of the single domain case in which rotation about a second axis is considered. Thus we have six rotation matrices operating on the initial vector. The case of a 180^{o} Bloch wall is a fairly simple example since 2γ changes only in sign and not in magnitude. The working of this example is tedius and we merely quote the result neglecting terms in $\sin^{3}2\gamma$ and higher powers. This is justifiable because ρ_{o} is much less than δ_{o} (see Kurtzig (62)). Thus

$$|\lambda| = \tfrac{1}{2}\tan^{-1}\left[\frac{\sin 2\gamma[\sin(\Delta - \Delta') - 2\sin\Delta'(1 - \cos\Delta)]}{1 - \sin^{2}2\gamma(3 + \cos\Delta\cos\Delta' - \sin\Delta\sin\Delta' - 2\cos\Delta - 2\cos\Delta')}\right]$$

7.4 The Transmission Matrix Method

Here we follow the notation and procedure of Fathers and Tanner (63) in their paper on inclined domain walls. Assuming a plane wave solution of the form

$$\underline{E} = \underline{E}o \exp i\omega (t - \underline{n}.\underline{r}/c)$$

Maxwell's equations for a non-conducting homogeneous linear medium have solutions of the form

$$\underline{n}(\underline{n}.[\gamma]\underline{D}) - n^2[\gamma]\underline{D} + \underline{D} = 0 \qquad 3$$

where the $[\gamma]$ $(= [\epsilon]^{-1})$ tensor is given by

$$[\gamma] = \begin{bmatrix} \gamma_{11} & \{\gamma_{12} \pm i\gamma'_{12}\} & \gamma_{13} \\ \{\gamma_{12} \mp i\gamma'_{12}\} & \gamma_{22} & \gamma_{23} \\ \gamma_{13} & \gamma_{23} & \gamma_{33} \end{bmatrix} \qquad 4$$

Here the imaginary antisymmetric components depend on the magnetization, the upper signs referring to magnetization in the positive and the lower signs to magnetization in the negative direction. Solution of equation 3 subject to equation 4 with normalization yields the following Jones vectors.

$$D_+^{\pm z} = \begin{bmatrix} \cos\theta \\ \sin\theta \exp(\pm i\chi) \end{bmatrix} \quad D_-^{\pm z} = \begin{bmatrix} -\sin\theta \\ \cos\theta \exp(\mp i\chi) \end{bmatrix} \qquad 5$$

where $\tan\theta = \frac{\gamma_{22} - \gamma_{11}}{2\xi} + \left[\left(\frac{\gamma_{22} - \gamma_{11}}{2\xi}\right)^2 + 1\right]^{\frac{1}{2}}$

and $\gamma_{12} + i\gamma'_{12} = \xi \exp(i\chi)$ ie. $\chi = \tan^{-1}\gamma'_{12}/\gamma_{12}$

The superscripts in equation 5 refer to the magnetization direction and the subscripts to the value of n associated with the normal mode. Any polarization state may be represented as a linear combination of these vectors as

$$D = A_+D_+ + A_-D_-$$

The amplitudes at two points on the wave may be related by a transmission matrix M as

$$\begin{bmatrix} A_+ \\ A_- \end{bmatrix}_{z=L} = M \begin{bmatrix} A_+ \\ A_- \end{bmatrix}_{z=0}$$

where $$M = \begin{bmatrix} \exp(i\phi) & 0 \\ 0 & \exp(-i\phi) \end{bmatrix} \qquad 6$$

and $$\phi = -\tfrac{1}{2}(|K_+| - |K_-|)L$$

K_+ and K_- are the wave vectors of the two normal modes and L is the path length in the crystal. Transforming equation 6 into a basis of linearly polarized modes we obtain a matrix describing the x and y components of D

$$M = \begin{bmatrix} \cos\phi + i\sin\phi\cos 2\theta & i\sin\phi\sin 2\theta\exp(\mp i\chi) \\ i\sin\phi\sin 2\theta\exp(\pm i\chi) & \cos\phi - i\sin\phi\cos 2\theta \end{bmatrix}$$

7.4.1 The Single Domain Case

In most practical cases the incident wave is linearly polarized and may be represented by

$$D_o = \begin{bmatrix} \cos\beta \\ \sin\beta \end{bmatrix}$$

where β is the angle of the polarization to the y axis. Taking $\beta=0$ and $\chi=\pi/2$ (a valid assumption since the axes of the tensor are quite arbitrary) we find the final state to be given by

$$\begin{bmatrix} \cos\phi + i\sin\phi\cos 2\theta \\ \pm \sin 2\theta \sin\phi \end{bmatrix}$$

Interpreting this vector in the usual way (see for example Cornbleet (64)) the angle between the major axis and the y axis is given by

$$|\lambda| = \tfrac{1}{2}\tan^{-1}\left[\frac{\sin 2\theta \sin 2\phi}{1 - 2\sin^2 2\theta \sin^2\phi}\right]$$

7.4.2 The Two Domain Case

In this case there are two transmission matices for magnetization in the +z and -z directions.

$$M = \begin{bmatrix} \cos\phi + i\sin\phi\cos 2\theta & \mp \sin\phi\sin 2\theta \\ \pm\sin\phi\sin 2\theta & \cos\phi - i\sin\phi\cos 2\theta \end{bmatrix}$$

$$M' = \begin{bmatrix} \cos\phi' + i\sin\phi'\cos 2\theta & \pm\sin\phi'\sin 2\theta \\ \mp \sin\phi'\sin 2\theta & \cos\phi' - i\sin\phi'\cos 2\theta \end{bmatrix}$$

where $\phi = -\tfrac{1}{2}(|K_+| - |K_-|)\ d$

and $$\phi' = -\tfrac{1}{2}(|K_+| - |K_-|)(L - d)$$

where d is the depth of the Bloch wall. Once again we will just quote the result neglecting terms in sin 2θ and higher powers.

$$|\lambda| = \tfrac{1}{2}\tan^{-1}\left[\frac{\sin 2\theta\,[\sin 2(\phi - \phi') - 4\sin^2\phi\sin 2\phi']}{1 - \sin^2 2\theta(8\sin^2\phi\sin^2\phi' - 4\sin\phi\sin\phi'\cos\phi\cos\phi' + 2\sin^2\phi'\cos^2\phi + 2\sin^2\phi\cos^2\phi')}\right]$$

7.5 Discussion

In our calculations using the Poincaré sphere and matrix methods we have used the notations of Ramachandran and Ramaseshan and Fathers and Tanner respectively. In fact by definition $\Delta = -2\phi$ and $2\chi = 2\theta$. The latter is by virtue of the way the Poincaré sphere is constructed (see for example Wahlstrom (65)). Thus the results are identical.

Kurtzig (62) has already used the single domain formula calculated by the Poincaré sphere representation to separate the Faraday rotation and birefringent components in $FeBO_3$. To illustrate this we put our single domain result in the form used by Kurtzig. The assumption is made that the Faraday rotation is small compared with the birefringence. This leads to two approximations. Firstly the denominator

approaches unity and secondly $\sin 2\gamma$ (= $\sin 2\theta$) approaches $\tan 2\gamma$. Taking our single domain result and substituting

$$\Delta = (2\pi/360)B(A)d/\cos A, \quad \delta_0 = (2\pi/360)B(A), \quad \varrho_0 = Fo \sin A$$

where d is the crystal thickness and A is the angle between the direction of propogation and the c-axis, we obtain in the form used by Kurtzig

$$\lambda \doteq \frac{180Fo \sin A}{\pi B(A)} \sin\left[\frac{\pi B(A)d}{180\cos A}\right]$$

If λ is measured as a function of A curve matching enables one to separate Fo and B(A). In principle it should be possible to demonstrate the presence of an in-plane Bloch wall using this method. Recently Haisma, Prins and van Mierloo (66) in a paper on the refractive indices of $FeBO_3$ have suggested that the presence of a Bloch wall does not effect the measured values if the measurement is carried out under conditions such that $\pi B(A)d/180\cos A = n\pi$ i.e. $\lambda = 0$. They use this formula in the derivation of a formula for the refractive indices and, since the condition is different in the presence of a Bloch wall, it is difficult to see how the measured values would be unaffected.

There seems to be little to choose between the two methods for magneto-optical calculation but the use of both does assist in eliminating errors.

Appendix

Bernal, Struck and White (67) give the following atomic positions for $FeBO_3$ in the triply primative hexagonal cell:

$$(0,\ 0,\ 0;\ \tfrac{1}{3},\tfrac{2}{3},\ \tfrac{2}{3};\ \tfrac{2}{3},\ \tfrac{1}{3},\ \tfrac{1}{3})\ +$$

6 Fe in $0,\ 0,\ 0;\ 0,\ 0,\ \tfrac{1}{2}$;

6 B in $0,\ 0,\ \tfrac{1}{4};\ 0,\ 0,\ \tfrac{3}{4}$;

18 O in $\pm x,\ 0,\ \tfrac{1}{4};\ 0,\ x,\ \tfrac{1}{4};\ \bar{x},\ \bar{x},\tfrac{1}{4}$ with $x = 0.29$

For the symmetric Laue case the extinction distance is given by the reciprocal of the diameter of the dispersion surface hyperbola. This diameter is given by (Batterman and Cole (14)).

$$k\Gamma\,|C|\,F_g\,\sec\theta$$

For the 110 reflection this yields extinction distances of about 6.5 μm and 3.0μm for MoKα and CuKα respectively.

References

1. C.S. Barrett: Phys. Rev. 38, 832 (1931)
2. L.G. Schulz: Trans. AIME 200, 1082 (1954)
3. A. Guinier and J. Tennevin: Acta. Cryst. 2, 133 (1949)
4. W.F. Berg: Naturwissenschaften 19,391 (1931)
5. C.S Barrett: Trans. AIME 15,161 (1945)
6. W.L Bond and J. Andrus: Amer. Mineralogist 37,622 (1952)
7. U. Bonse and E. Kappler: Z. Naturforsch. 13a,348 (1958)
8. M. Hart: Science Progress (Oxford) 56,429 (1968)
9. A.R Lang: Modern Diffraction and Imaging Techniques in Material Science Ed. Amelinckx, North-Holland (1970)
10. B.K Tanner: X-Ray Diffraction Topography (1977) Pergamon
11. C.G. Darwin: Phil. Mag. 27,315 (1914); 27,675 (1914)
12. P.P Ewald: Ann. Physik 49,1 (1916); 49,117 (1916); 54,519 (1917); Acta. Cryst. 11,888 (1958)
13. M.v. Laue: Ergeb. Exakt. Naturew. 10,133 (1931)
14. B. W Batterman and H. Cole: Rev. Mod. Phys. 36(3) 681 (1964)
15. M. Hart: Rep. Prog. Phys. 34,435 (1971)
16. N. Kato: Acta. Cryst. 11,885 (1958)
17. N. Kato: Acta. Cryst. 13,349 (1960)
18. T. Tuomi, K. Naukkarinen, E. Laurila and P. Rabe: Acta polytech. Scand. Ph 100,1 (1973)
19. T. Tuomi, K. Naukkarinen and P. Rabe: Phys. Stat.Sol. (a) 25,93 (1974)
20. M. Hart: J. Appl. Cryst. 8,436 (1975)
21. J. Bordas, A.M. Glazer and H. Hauser: Phil.Mag.32,471 (1975)

22. A. Authier:Advance. X-ray Anal. 10,9 (1967)

23. B. K Tanner: D. Phil. Thesis, Oxford Univ. (1971)

24. B. K Tanner, M. Safa and D. Midgley: J. Appl. Cryst. 10,91 (1977)

25. M. Safa, D. Midgley and B.K Tanner: Phys. Stat. Sol. (a) 28,K89 (1975)

26. A. Mathiot, J.F. Petroff and Y. Bernard: Phys. Stat. Sol. (a) 20, K1 - K3 (1973)

27. J.F Petroff and A. Mathiot: Mater. Res. Bull. 9,319 (1974)

28. A. Mathiot and J.F Petroff: AIP Conf. Proc. 13,757 (1975)

29. W.D. Corner and T.S. Al-Bassam: J. Phys C. 4,47 (1971)

30. M.M Hornreich: Intermag. Conference (Kyoto 1972)

31. J.D Cashion, A.H. Cooke, M.J.M. Leask, T.L. Thorp and M.R Wells: J. Mat.Sci. 3,402 (1968)

32. B.M. Wanklyn, F.R. Wondre, G.B. Ansell and W. Davison: J. Mater. Sci. 9,2007 (1974)

33. B.M. Wanklyn, D. Midgley and B.K. Tanner: J. Cryst. Growth, 29,281 (1975)

34. I.M. Coe and D. Elwell: J. Cryst. Growth, 23,345 (1974)

35. S. Ikeno, H. Maruyama and N. Kato: J. Cryst. Growth, 3/4,683 (1968)

36. R.A Duckett and A.R. Lang: J. Cryst. Growth 18,135 (1972)

37. H. Klapper: J. Cryst. Growth, 10,13 (1971)

38. H. Klapper: J. Cryst. Growth 15,281 (1972)

39. H. Klapper: Phys. Stat. Sol. (a) 14,99 (1972)

40. H. Klapper: Phys. Stat. Sol. (a) 14,443 (1972)

41. H. Klapper: Z. Naturf. 28a,614 (1973)

42. H. Klapper: Acta cryst. A,31,S212 (1975)

43. H. Klapper and H. Küppers: Acta cryst. A,29,495 (1973)

44. H. Klapper and H. Küppers: Acta cryst. A,30,302 (1974)

45. H. Klapper, M. Fishman and V.G. Lutsau: Phys. Stat. Sol. (a) 21,115 (1974)

46. M. Safa, B.K Tanner, H. Klapper and B.M. Wanklyn: Phil.Mag. 35,3,811 (1977)

47. R.S. Fiegelson: J. Amer. Ceram. Soc. 50,433 (1967)

48. S.H. Smith and B.M. Wanklyn: J. Cryst. Growth, 21,23 (1974)

49. R. Englman: The Jahn-Teller Effect in Molecules and Crystals (1972) Wiley

50. S.J. Allen: Phys. Rev. 166,530 (1968)

51. E. Pytte: Phys. Rev. 3,B3503 (1971)

52. G.A. Gehring and K.A. Gehring: Rep. Prog. Phys. 38,1 (1975)

53. A.H. Cooke, C.J. Ellis, K.A. Gehring, M.J.M. Leask, D.M. Martin, B.M. Wanklyn, M.R. Wells, R.L. White: Solid St. Commun. 8,689 (1970)

54. P.J. Becker and J. Laugsch: Phys.Stat. Sol. (b) 44 K109 (1971)

55. F. Sayetat, J.X. Boucherle, M. Belakhovsky, A. Kullel, F. Tcheou, H. Fuess: Phys. Lett.34A,361 (1971)

56. K.A. Gehring and H.M. Rosenberg: Phys. Stat. Sol. (b) 47 K75 (1971)

57. M.J.M. Leaske, K.J. Maxwell, R.N. Tyte, P.J. Becker, A. Kasten and W. Wuchner: Solid St. Commun. 9,1707 (1973)

58. D.E. Lacklison, J. Chadwick and J.L. Page: J. Phys. D 5,810 (1972)

59. J. Haisma and W.T. Stacy: J. Appl. Phys. 39,922 (1973)

60. G.N. Ramachandran and S. Rameshan: J. Opt. Soc. Am. 42,1,49 (1952)

61. G. Szivessy: Handbuch der Physic Vol. 20 Julius Springer, Berlin

62. A.J. Kurtzig: J. Appl. Phys. 42,9,3494 (1971)

63. D.J. Fathers and B.K. Tanner: Phil. Mag. 27,1,17 (1973)

64. S. Cornbleet: Microwave Optics Academic Press

65. E.E. Wahlstrom: Optical Crystallography Wiley

66. J. Haisma, H.J. Prins and K.L.L. van Mierloo: J. Appl. Phys. 7,162 (1974)

67 I. Bernal, C W Struck and J .G White: Acta. Cryst. 16.849 (1963)